The Astrophysical Journal, 908:193 (19pp), 2021 February 20 https://doi.org/10.3847/1538-4357/abd6c2

Particle Acceleration by Relativistic Magnetic Reconnection Driven by Kink Instability Turbulence in Poynting Flux–Dominated Jets

Tania E. Medina-Torrejón[1], Elisabete M. de Gouveia Dal Pino[2], Luis H. S. Kadowaki[2], Grzegorz Kowal[3], Chandra B. Singh[4], and Yosuke Mizuno[5,6]
[1] Universidade de São Paulo, Instituto de Física, São Paulo, Brazil
[2] Universidade de São Paulo, Instituto de Astronomia, Geofísica e Ciências Atmosféricas, Departamento de Astronomia, 1226 Matão Street, 05508-090 São Paulo, Brazil; dalpino@iag.usp.br
[3] Escola de Artes, Ciências e Humanidades–Universidade de São Paulo, Av. Arlindo Béttio, 1000—Vila Guaraciaba, 03828-000 São Paulo, Brazil
[4] South-Western Institute for Astronomy Research, Yunnan University, University Town, Chenggong District, Kunming 650500, People's Republic of China
[5] Tsung-Dao Lee Institute and School of Physics and Astronomy, Shanghai Jiao Tong University, 200240 Shanghai, People's Republic of China
[6] Institut für Theoretische Physik, Goethe Universität, D-60438 Frankfurt am Main, Germany
Received 2020 September 16; revised 2020 December 9; accepted 2020 December 22; published 2021 February 24

Abstract

Particle acceleration in magnetized relativistic jets still puzzles theorists. In this work, we investigate the acceleration of particles injected into a three-dimensional relativistic magnetohydrodynamical jet subject to current-driven kink (CDK) instability. We find that, once turbulence driven by CDK fully develops, achieving a nearly stationary state, the amplitude of excited wiggles along the jet spine attains maximum growth, causing disruption of the magnetic field lines and the formation of several sites of fast reconnection. Low-energy protons injected into the jet at this state experience exponential acceleration, mostly in directions parallel to the local magnetic field, up to maximum energies $E \sim 10^{16}$ eV for $B \sim 0.1$ G and $E \sim 10^{18}$ eV for $B \sim 10$ G. The Larmor radius of the particles attaining these energies corresponds to the size of the acceleration region (∼the diameter of the perturbed jet). There is a clear association of the accelerated particles with regions of fast reconnection. In the early nonlinear growth stage of the CDK, when there are no sites of fast reconnection yet, injected particles with initially much larger energy are accelerated by magnetic curvature drift. We have also obtained the acceleration time due to reconnection with a dependence on the particles' energy, $t_A \propto E^{0.1}$. The energy spectrum of the accelerated particles develops a power-law index $p \sim -1.2$ in the beginning, in agreement with earlier works. Our results provide a multidimensional framework for exploring this process in real systems and explain their emission patterns, especially at very high energies, and associated neutrino emission recently detected in some blazars.

Unified Astronomy Thesaurus concepts: Magnetohydrodynamical simulations (1966); Particle astrophysics (96); High energy astrophysics (739); Magnetohydrodynamics (1964); Cosmic rays (329)

1. Introduction

Relativistic, collimated jets are ubiquitous in extreme astrophysical sources like microquasars (black hole X-ray binary system), active galactic nuclei (AGNs), and gamma-ray bursts (GRBs). An important property common to all of these classes of objects is the required presence of magnetic fields to allow the formation of these jets (e.g., Blandford & Znajek 1977; Blandford & Payne 1982). Observed polarized nonthermal emission in all wavelengths is also evidence that these jets are highly magnetized, especially near the launching region at the source (e.g., Laurent et al. 2011; Doeleman et al. 2012; Martí-Vidal et al. 2015). In particular, there has been reported evidence of a helical magnetic field feature in the M87 jet (Harris et al. 2003). General relativistic magnetohydrodynamic (GRMHD) simulations with accretion disks around the spinning black hole of these sources are compatible with the observations and the proposed mechanisms for jet formation. They reveal the formation of a Poynting flux–dominated jet spine with a large Lorentz factor surrounded by a mildly relativistic (matter-dominated) sheath and a subrelativistic wind (e.g., McKinney 2006; Hardee et al. 2007; Abramowicz & Fragile 2013; Yuan & Narayan 2014). This spine–sheath structure has indeed been inferred in very long baseline interferometry observations from nearby FR I and FR II radio galaxies like M87 (Kovalev et al. 2007), 3C 84 (Nagai et al. 2014), and Cyg A (Boccardi et al. 2015), as well as in blazars like Mrk 501 (Giroletti et al. 2004) and 3C 273 (Lobanov & Zensus 2001).

Another important constraint from the observations is the fact that at distances large enough from the sources, these jets should become kinetically dominated, and as such, they should convert most of the magnetic energy into kinetic. A mechanism that could favor such conversion in jets is magnetic reconnection (e.g., Giannios 2010; de Gouveia Dal Pino & Kowal 2015; de Gouveia Dal Pino et al. 2018; Werner et al. 2018, and references therein). Lately, this process has been largely investigated in the framework of compact sources like pulsar nebulae (e.g., Lyubarsky & Kirk 2001; Clausen-Brown & Lyutikov 2012; Cerutti et al. 2014; Sironi & Spitkovsky 2014), GRBs (e.g., Drenkhahn & Spruit 2002; Giannios & Spruit 2007; Zhang & Yan 2011), and jets and accretion flows around black holes (e.g., de Gouveia Dal Pino & Lazarian 2005; Giannios et al. 2009; de Gouveia Dal Pino et al. 2010b, 2010a; Giannios 2010; McKinney & Uzdensky 2012; Kadowaki et al. 2015; Khiali et al. 2015; Singh et al. 2015; Sironi et al. 2015; Singh et al. 2016; de Gouveia Dal Pino et al. 2018; Kadowaki et al. 2018b, 2018a; Rodriguez-Ramirez et al. 2019; Christie et al. 2019; Fowler et al. 2019; Giannios & Uzdensky 2019; Nishikawa et al. 2020; Nathanail et al. 2020; Davelaar et al. 2020).

Among all classes of relativistic jets, reconnection can be particularly important in blazars, which are a subclass of AGNs with jets making very small angles with our line of sight. This geometry is particularly favorable, since relativistic effects, like Doppler boosting with apparent enhancement of the observed

emission, are maximized. Blazars produce usually highly variable, nonthermal emission in all wavelengths, which is generally attributed to relativistic particles (protons and electrons) accelerated stochastically in recollimation shocks along the jet and in its head (e.g., Mizuno et al. 2015; Hovatta & Lindfors 2019; Matthews et al. 2020). However, there is increasing evidence that shock acceleration may not always be as efficient in the magnetically dominated regions of these jets, particularly to explain the very high energy (VHE) emission (Sironi et al. 2013; de Gouveia Dal Pino & Kowal 2015; Bell et al. 2018). This may be the case, for instance, for the blazars PKS 2155–304 (Aharonian et al. 2007) and Mrk 501 (Albert et al. 2007; see also 3C 279 in Ackermann et al. 2016 and 3C 54.3 in Britto et al. 2016). They produce very short duration gamma-ray flares of minutes at the TeV band that imply extremely compact acceleration/emission regions ($<R_S/c$, where R_S is the Schwartzschild radius) with Lorentz factors much larger than the typical jet bulk values in these sources (which are $\Gamma \simeq 5$–10). This is the only way to prevent the reabsorption of the gamma rays within the source due to electron–positron pair creation (e.g., Begelman et al. 2008). The only mechanism that seems to be able to drive both the high variability and compactness of the TeV emission is fast magnetic reconnection involving misaligned current sheets inside the jet (Giannios et al. 2009; Giannios 2013; Kushwaha et al. 2017). A similar mechanism has also been invoked to explain the prompt emission in GRBs (e.g., Giannios 2008; Zhang & Yan 2011). Moreover, the recent simultaneous detection of gamma rays and high-energy neutrinos from the blazar TXS 0506+056 (Aartsen et al. 2018) is evidence of the presence of high-energy protons interacting with ambient photons, producing pions and a subsequent decay in gamma rays and neutrinos. It has been argued that if these protons are produced in magnetically dominated regions of the jet near the core, then they are probably accelerated by fast magnetic reconnection (e.g., de Gouveia Dal Pino et al. 2018).

Magnetic reconnection is produced from the merging of two magnetic fluxes of opposite polarity. This causes partial breaking and rearrangement of the field topology, and it is fast when its rate V_R is a substantial fraction of the local Alfvén speed V_A (e.g., Zweibel & Yamada 2009; Lazarian et al. 2012, 2020). The ubiquitous turbulence in astrophysical flows is acknowledged as one of the main driving mechanisms of fast reconnection due to the wandering of the magnetic field lines that allows for many simultaneous events of reconnection and the broadening of the outflow region removing the reconnected flux more efficiently. These two factors result in the reconnection rate being independent of the small microscopic magnetic resistivity (Lazarian & Vishniac 1999; Eyink et al. 2011; Kowal et al. 2009; Takamoto et al. 2015; Santos-Lima et al. 2010, 2020).

The breaking and rearrangement of the reconnected lines causes the conversion of magnetic energy into kinetic energy and particle acceleration. De Gouveia Dal Pino & Lazarian (2005) realized that particles could be accelerated in a fast magnetic reconnection site in a similar way as in diffusive shock acceleration (Blandford & Eichler 1987; Bell 1978). In other words, particles bouncing back and forth between two converging magnetic fluxes of opposite polarity in a reconnection discontinuity (or current sheet) gain energy due to head-on collisions with magnetic fluctuations at a rate $\Delta E/E \propto V_R/c$, which implies a first-order Fermi process. This has been successfully tested numerically (see, e.g., Drake et al. 2006; Kowal et al. 2011, 2012). Kowal et al. (2011), in particular, demonstrated by means of two- and three-dimensional (2D and 3D) MHD simulations with test particles, the equivalence between this process and that of particles being accelerated within 2D merging magnetic islands (or plasmoids) excited, e.g., by tearing mode instability. It is important to remark that magnetic islands are actually the 2D cross sections of the 3D flux tube, and in real systems reconnection is 3D and thus particles accelerate in 3D reconnection sites (e.g., Kowal et al. 2011; de Gouveia Dal Pino & Kowal 2015).

The realization that reconnection acceleration can be a fundamental mechanism to explain observed nonthermal, highly variable emission, especially at VHEs, in magnetically dominated sources has motivated intensive study mainly through 2D and 3D particle-in-cell (PIC) simulations of current sheets in a slab geometry in collisionless plasmas (e.g., Drake et al. 2006; Zenitani & Hoshino 2001, 2007, 2008; Lyubarsky & Liverts 2008; Drake et al. 2010; Clausen-Brown & Lyutikov 2012; Cerutti et al. 2012; Li et al. 2015; Lyutikov et al. 2017; Werner et al. 2018, 2019; Sironi & Spitkovsky 2014; Guo et al. 2015, 2016). These studies have probed the kinetic scales of the process. To assess the stochastic Fermi mechanism at the macroscopic scales of collisional flows present in most astrophysical systems, the tracking of test particle distributions in such flows is also a very useful and complementary tool to help in the understanding of the overall process across the scales. Such studies have been performed combining 2D and 3D MHD simulations with the injection of thousands of test particles into the reconnection domain (Kowal et al. 2011, 2012; del Valle et al. 2016; Beresnyak & Li 2016; de Gouveia Dal Pino et al. 2018, 2020). In particular, Kowal et al. (2012) distinguished the first-order Fermi process that occurs inside large-scale current sheets with embedded turbulence driving fast reconnection from a second-order Fermi process occurring in pure turbulent environments (see also Brunetti & Lazarian 2011; Brunetti & Vazza 2020).[7] Both PIC and test particle+MHD approaches have probed the efficiency of the stochastic reconnection acceleration, particularly in three dimensions, with exponential growth of the particle energy in time, implying a power-law energy dependence of the acceleration rate and the production of an extended, nonthermal distribution of relativistic particles with a power-law tail (e.g., del Valle et al. 2016).

The results above are applicable to magnetized astrophysical flows in general and especially to relativistic jets in regions near the source where they are possibly magnetically dominated. The investigation of magnetic reconnection acceleration in these objects is the aim of the present work.

[7] It is worth noting that in a more recent PIC study, Comisso & Sironi (2018, 2019) also considered a pure turbulent, magnetically dominated system but with no guide field and found that particles are initially exponentially accelerated in small-scale reconnecting current sheets and then undergo further acceleration by stochastic interactions with the turbulent fluctuations at a slower rate. This is, in principle, similar to the process described above, especially in Kowal et al. (2012; see their Figure 1, bottom panel). But in an MHD environment, the presence of turbulence naturally leads to fast reconnection with the formation of 3D current sheets in the entire turbulent domain (Lazarian-Vishniac theory; Lazarian & Vishniac 1999) and stochastic particle acceleration in these sites, as described previously. A key difference between the Comisso & Sironi (2018, 2019) simulations and those of Kowal et al. (2012; and the ones in the present work) is that in the latter, there is the underlying large-scale magnetic field that favors the confinement of the particles in the regions where the current sheets are formed; thus, the exponential acceleration can be sustained longer and not only during the initial stages.

The presence of instabilities in the jet can drive turbulence and thus fast magnetic reconnection (e.g., Spruit et al. 2001; Barniol Duran et al. 2017; de Gouveia Dal Pino et al. 2018; Gill et al. 2018). In particular, jets with helical magnetic field structure can be subject to current-driven kink (CDK) instability (e.g., Begelman 1998; Giannios & Spruit 2006; Mizuno et al. 2009, 2011, 2012, 2014; Das & Begelman 2019), and a number of recent numerical works have revealed that this instability can operate in the jet spine without disrupting the entire jet structure, converting magnetic into kinetic energy and driving reconnection (Porth & Komissarov 2015; Singh et al. 2016; Bromberg & Tchekhovskoy 2016; Tchekhovskoy & Bromberg 2016; Striani et al. 2016; Bromberg et al. 2019; Davelaar et al. 2020). In particular, in their 3D relativistic MHD (RMHD) simulations of Poynting flux–dominated rotating jets with helical fields, Singh et al. (2016) verified that the CDK-induced turbulence triggers the formation of current sheets with fast reconnection rates of $\sim 0.05 V_A$.

In a companion work to the present one (Kadowaki et al. 2020, hereafter KGM20), we have expanded upon the previous studies above, applying a magnetic reconnection search algorithm developed in Kadowaki et al. (2018b; see also Zhdankin et al. 2013) to a simulated 3D RMHD jet with a helical field (as in Singh et al. 2016). With this study, we have been able to identify several sites of reconnection and obtain robust values of the reconnection rates and magnetic power of every reconnection event inside the jet in different snapshots, as well as the topological characteristics of each reconnection region (see also Kadowaki et al. 2018a). In the present work, in order to obtain a full understanding of how this magnetic energy released by the CDK instability can be channeled into energetic nonthermal particles in the fast reconnection regions, we present a study of in situ particle acceleration by injecting hundreds to thousands of test particles into the same 3D RMHD jet model we employed in KGM20.

We should remark that the preliminary results of this study have been presented in de Gouveia Dal Pino et al. (2018, 2020). Other recent studies based on PIC simulations of relativistic jets have also explored particle acceleration in relativistic jets (e.g., Alves et al. 2018; Nishikawa et al. 2020; Davelaar et al. 2020). Alves et al. (2018) investigated particle acceleration in the early nonlinear stage of the CDK instability, before the development of turbulence, and verified that particles are accelerated by magnetic curvature drift. We have also identified this process in our simulations in the early stages of the CDK growth, but it is soon replaced by reconnection acceleration when turbulence settles in the system (see below). Davelaar et al. (2020), on the other hand, in their simulations with high magnetization, detected only the acceleration by magnetic reconnection. Nishikawa et al. (2020) explored particle acceleration in a 3D PIC relativistic jet interacting with the environment considering different driving mechanisms of turbulence inside the jet, such as Weibel, kinetic Kelvin–Helmholtz, and mushroom instabilities, and they also concluded that magnetic reconnection is the dominant acceleration process.

We organize this paper as follows. In Section 2, we describe the numerical method and our setup for both the RMHD jet simulations and the test particle method. In Section 3, we present our numerical results of the development of reconnection and the injection of test particles into the entire jet domain subject to the CDK instability and obtain the properties of the acceleration, such as the particles' energy growth with time, the acceleration rates, and the particles' spectrum, as well as the connections of the accelerated particles with the reconnection regions (identified in KGM20). Finally, in Section 4, we discuss our findings and draw our conclusions.

2. Numerical Method and Setup

Following Kowal et al. (2011, 2012) and del Valle et al. (2016; see also de Gouveia Dal Pino & Kowal 2015), we inject test particles (100–10,000 protons) into frozen-in-time 3D MHD domains in order to test particle acceleration by magnetic reconnection. However, instead of taking a large-scale single current sheet with embedded controlled weak stochastic turbulence, as in these previous works, here we consider in situ particle acceleration in a relativistic 3D MHD jet where turbulence and fast magnetic reconnection are naturally induced by CDK instability (Singh et al. 2016). As in Kowal et al. (2011, 2012), we can neglect the macroscopic MHD dynamical time variations (see further justification for this in Section 4), and, once the instability reaches saturation and turbulence is fully developed with the appearance of several sites of fast reconnection in the jet, we can inject test particles into a snapshot to follow their acceleration. In fact, we show that particles undergo acceleration mostly in the reconnected regions once this condition is fulfilled.

2.1. 3D MHD Jet Simulation Setup

As in Singh et al. (2016), we perform RMHD simulations using the 3D GRMHD code RAISHIN (Mizuno et al. 2006, 2011, 2014). A preexisting jet is established across the computational domain (tower jet). We use a similar parameterization as in model $D2$ of Singh et al. (2016), which has a rotating jet with an initial force-free helical magnetic field and decreasing radial density profile.

Table 1 gives the initial conditions for the jet model. The computational domain is $6L \times 6L \times 6L$ in a Cartesian (x, y, z) coordinate system, where L is the length scale unit of the computation domain. We consider two different grid resolutions in the three directions: $\Delta L = L/40$, corresponding to 240 cells in each direction (model j240 in Table 1), and $\Delta L = L/80$, corresponding to 480 cells in each direction (model j480 in Table 1). Distinct from Singh et al. (2016), we impose outflow boundaries only in the transverse directions x and y and adopt periodic boundaries in the z direction in a similar way to the setup in Mizuno et al. (2012).

The code unit (c.u.) for the velocity is the speed of light c, the magnetic field is in units of $\sqrt{4\pi\rho_0 c^2}$, the density is in units of ρ_0 ($\rho_0 = 1$ in the code), the pressure is in units of $\rho_0 c^2$, and the time is in units of L/c.

The jet initial angular velocity is given by

$$\Omega = \begin{cases} \Omega_0 & \text{if } R \leqslant R_0 \\ \Omega_0 (R_0/R) & \text{if } R > R_0, \end{cases} \quad (1)$$

where R_0 is the radius of the jet core. In the simulations, $R_0 = (1/4)L$ and $\Omega_0 = 2.0\ L/c$.

The initial helical magnetic field has poloidal and toroidal components given, respectively, by

$$B_z = \frac{B_0}{1 + (R/R_0)^2}, \quad (2)$$

Table 1
Parameters for the MHD Simulations

Model	Resolution	$p_0[\rho_0 c^2]$	$B_0[\sqrt{4\pi\rho_0 c^2}]$	$\Omega_0[c/L]$	$R_0[L]$	σ
j240	240^3	0.02	0.7	2.0	0.25	0.6
j480	480^3	0.02	0.7	2.0	0.25	0.6

$$B_\phi = -\frac{B_0(R/R_0)[1 + (\Omega R_0)^2]^{1/2}}{1 + (R/R_0)^2}. \quad (3)$$

The initial poloidal and toroidal components of the drift velocity are given by

$$v_z = -\frac{B_\phi B_z}{B^2}\Omega R, \quad (4)$$

$$v_\phi = \left(1 - \frac{B_\phi^2}{B^2}\right)\Omega R. \quad (5)$$

The initial density profile decreases with the radius according to $\rho = \rho_1\sqrt{B^2/B_0^2}$, where $\rho_1 = 0.8\rho_0$ and the magnetic field amplitude is $B_0 = 0.7$.

The equation of state is given by $p = (\Gamma - 1)\rho e$, where Γ is the adiabatic index equal to $5/3$ and e is the specific internal energy density. We assume an initial gas pressure decreasing radially, similar to Equation (1),

$$p = \begin{cases} p_0 & \text{if } R \leqslant R_p \\ p_0(R_p/R) & \text{if } R > R_p, \end{cases} \quad (6)$$

with $R_p = (1/2)L$ and $p_0 = 0.02\,\rho_0 c^2$. These values correspond to an initial beta parameter $\beta = p_0/(B_0^2/8\pi) = 0.08$ and a magnetization parameter $\sigma = B_0^2/\gamma^2\rho h = 0.6$ (where h is the specific enthalpy) at the jet axis. The latter increases to maximum values around unity in more evolved times. We should remark that, although it is generally believed that the jet is highly magnetized at the launching site, the location of the region where effective acceleration and radiative dissipation occur is not yet well understood. Nevertheless, it is reasonable to suppose that an efficient reconnection acceleration and dissipation should occur when the magnetization has decreased to values $\gtrsim$1. This is, in fact, compatible with a recent proposal by Giannios & Uzdensky (2019). Here we explore a similar magnetization condition.

The initial profiles above are presented in Figure 1 in Singh et al. (2016) for $\Omega_0 = 2\ L/c$.

The code setup for spatial development of the CDK instability is the same as in Mizuno et al. (2012). In order to drive the instability and induce turbulence, a precession perturbation is applied by a radial velocity profile given by

$$\frac{v_R}{c} = \frac{\delta v}{N}\exp\left(-\frac{R}{R_a}\right)\sum_{n=1}^{N}\cos(m\theta)\sin\left(\frac{\pi n z}{L_z}\right), \quad (7)$$

where the amplitude of the perturbation is $\delta v = 0.01c$, $N = 8$, the radial width $R_a = 0.25L$, and we consider the mode $m = 1$ in order to induce the CDK instability.

2.2. Setup for Test Particle Acceleration

We inject test particles (protons) into a snapshot of RMHD jet simulations and integrate their trajectories using the GACCEL code (Kowal et al. 2011, 2012; del Valle et al. 2016), which solves the relativistic equation of motion of a charged particle,

$$\frac{d(\gamma m\boldsymbol{u})}{dt} = q(\boldsymbol{E} + \boldsymbol{u} \times \boldsymbol{B}), \quad (8)$$

where $\gamma \equiv (1 - u^2/c^2)^{-1}$ is the particle Lorentz factor, and $\boldsymbol{u}$, m, and q are the particle velocity, mass, and electric charge, respectively. The electric field is generated by the background flow of magnetized plasma and magnetic resistivity effects and can be obtained directly from the Ohm's law equation,

$$\boldsymbol{E} = -\boldsymbol{v} \times \boldsymbol{B} + \eta\boldsymbol{J}, \quad (9)$$

where $\boldsymbol{v}$ is the plasma velocity obtained from RMHD simulations. We neglect here the ohmic resistivity (second term on the right-hand side) in order to study the acceleration provided by the plasma magnetic fluctuations (first term on the right-hand side; Kowal et al. 2011, 2012).[8] Substituting Equation (9), the equation of motion (Equation (8)) is written as

$$\frac{d}{dt}(\gamma m\boldsymbol{u}) = q[(\boldsymbol{u} - \boldsymbol{v}) \times \boldsymbol{B}]. \quad (10)$$

The particle equation of motion (Equation (10)) is integrated using the fourth-order Runge–Kutta method, and the background plasma velocity $\boldsymbol{v}$ and magnetic field $\boldsymbol{B}$ at each step of the integration are obtained through linear interpolation of the values from the discrete grid of the MHD simulation domain.

We integrate Equation (10) for 100–10,000 protons with randomly chosen initial positions and directions of motion in the domain.[9] In most of the simulated models, we assume an initial Maxwellian distribution for the particle velocities corresponding to a temperature of 10^{10} K (nonrelativistic particles) and a mean kinetic energy of the order of 1 MeV ($\sim 10^{-3}\ m_p c^2$). Only in one of the models investigated, we have assumed an initial monoenergetic distribution, *ut25o* (see Table 2 and Section 3.2.2).

In order to check potential boundary effects, the trajectories of the particles are integrated considering two different boundary conditions: periodic in all directions (test particle model names ending with "p" in Table 2) and periodic in the z direction only with outflow boundaries in the x and y directions (test particle model names ending with "o" in Table 2) as in the simulated MHD background. In the first case, the particles are reinjected into the domain whenever they cross any jet boundary, while in the second case, they are reinjected only when they cross the periodic boundary of the jet (in the z direction). The results, as we will see in Section 3.2.6, are very similar in both cases, but the first implies much longer computing time.

[8] We note that the resistive term can be important only in the initial phases of the particle acceleration in the reconnection regions, but it is soon dominated by the first term, once the particles' Larmor radius becomes as large as the size of the magnetic fluctuations (e.g., Kowal et al. 2012).

[9] We have found that the results are very similar whether the particles are injected into a specific region of the jet with a large concentration of reconnection sites or the entire jet.

Table 2
Parameters for the Test Particles

Test	Jet Snapshot	N	B_0	x and y Boundaries	Initial Distribution	Jet Resolution
t25o	25	1000	0.094	Outflow	Maxwellian	240^3
ut25o	25	1000	0.094	Outflow	Monoenergetic	240^3
t30o	30	1000	0.094	Outflow	Maxwellian	240^3
t40o	40	5000	0.094	Outflow	Maxwellian	240^3
t44o	44	5000	0.094	Outflow	Maxwellian	240^3
t46o	46	1000	0.094	Outflow	Maxwellian	240^3
t50o	50	10,000	0.094	Outflow	Maxwellian	240^3
t50p	50	1000	0.094	Periodic	Maxwellian	240^3
9t50p	50	100	9.4	Periodic	Maxwellian	240^3
480t50o	50	1000	0.094	Outflow	Maxwellian	480^3

As we have described in Section 2.1, the background jet simulation is performed in c.u., but in the GACCEL code, we assume physical units. The adopted time unit is 1 hr, the velocity unit is the light speed c, and for the magnetic field, we adopt two possible values that correspond to the initial magnetic field in the jet axis, that is, $B_0 = 0.094$ and 9.4 G. These values come from converting the c.u. for the magnetic field strength, $B_0 = 0.7$ c.u., or $B_0 = 0.7\sqrt{4\pi\rho_0 c^2}$, assuming $\rho_0 = 1.0$ cm^{-3} and 10^4, respectively.

The initial and boundary conditions, as well as the number of particles considered for each test particle simulation, are presented in Table 2. The table also shows the chosen snapshots of the simulated jet in which the particles have been injected, $t = 25$, 30, 40, 44, 46, and 50 L/c, and the corresponding initial magnetic field at the jet axis (B_0). The simulated test particle models in the first column of the table are named according to the jet snapshot where the test particles were injected and the type of boundary condition of the injection in the x and y directions (either outflow or periodic).

In the current study, we do not include radiative losses, so the test particles can gain (or lose) energy only through the interactions with the moving magnetized plasma and its fluctuations.

We also note that the test particle simulations with GACCEL in the jet domain are extremely computer time–consuming, and for this reason, we have also performed a few runs initially injecting 100 particles only. In spite of the smaller number, the resulting particle acceleration rates and energy growth are similar to those obtained with 1000 and 10,000 particles injected. This is due to the fact that we allow the particles to be reinjected into the domain when crossing the boundaries, which naturally increases the number of interactions and thus helps to improve the statistics of the events. The reinjection of the particles in the z direction mimics the large extension of a real jet, since in our simulations, we only consider a small portion of it.

3. Results

We start by presenting the results of the 3D RMHD simulations of the relativistic jet, and then we describe the results of the injection of test particles into this domain in different snapshots along the jet evolution.

3.1. 3D MHD Simulation of the Relativistic Tower Jet

Figure 1 shows the time evolution of the relativistic jet (model j240 in Table 1) for snapshots at $t = 25$, 30, 40, 44, 46, and 50 L/c. Figure 1 depicts, in color scales, the isosurface of the magnetic current density intensity at half maximum in orange and the density map of the jet central slice (at the plane zy, and $x = 0$), as well as the magnetic field lines in black. As time evolves and the CDK instability grows, the jet spine becomes increasingly deformed and disruptive, driving turbulence and magnetic reconnection.

The resolution of our simulated jet is large enough to allow us to follow the growth of the turbulence and disentangle the reconnection structures. As described in Section 1, in a concomitant work (KGM20), we performed a systematic analysis of identification of all sites of magnetic reconnection in the evolving tower jet based on the algorithm developed in Kadowaki et al. (2018b; see Figures 1 and 2 of KGM20). The 2D cuts of the 3D reconnection sites give evidence of the presence of X points and extended chains of magnetic islands (see Figures 3 and 4 in KGM20). It has also been found that the distribution of the reconnection rates follows a lognormal behavior (see Figure 7 in KGM20), which is characteristic of turbulent flows, thus providing additional evidence that the turbulence (induced by the CDK instability) is driving the fast reconnection events (in agreement with the theory of Lazarian & Vishniac 1999; see also Kadowaki et al. 2018b; Santos-Lima et al. 2020) along the relativistic jet.

In Figure 1, the green dots characterize all sites of fast reconnection (identified with the search algorithm), that is, with reconnection velocities larger than or equal to the average reconnection rate obtained for each snapshot. Table 3 presents this average and the maximum reconnection velocity values for each of the snapshots of Figure 1 (in units of local Alfvén speed), as well as the number of reconnection sites (or counts) with reconnection velocities larger than the average value.

We note that in $t = 25$ L/c, there are no green dots (or reconnection regions) because turbulence and fast reconnection driven by the CDK instability have not developed yet, but in $t = 30$ L/c, we already identify the break of symmetry of the plasma column and the appearance of a few fast reconnection sites at the jet axis. We find that until near $t = 40$ L/c, there are still very few sites of fast reconnection, but in this snapshot and beyond, there are several sites spread over all of the jet domain, as we see in $t = 44$, 46, and 50 L/c in Figure 1. It is interesting that in the snapshot $t = 40$ L/c, though it presents several sites, the reconnection velocities are all around the average, contrary to what we see in the more evolved snapshots, where there are sites with very high reconnection speeds. In KGM20, these reconnection events are discussed in more detail, and an average reconnection velocity $\langle V_{\rm rec}/V_A\rangle \simeq 0.05$ is derived when accounting for all reconnection events in all snapshots

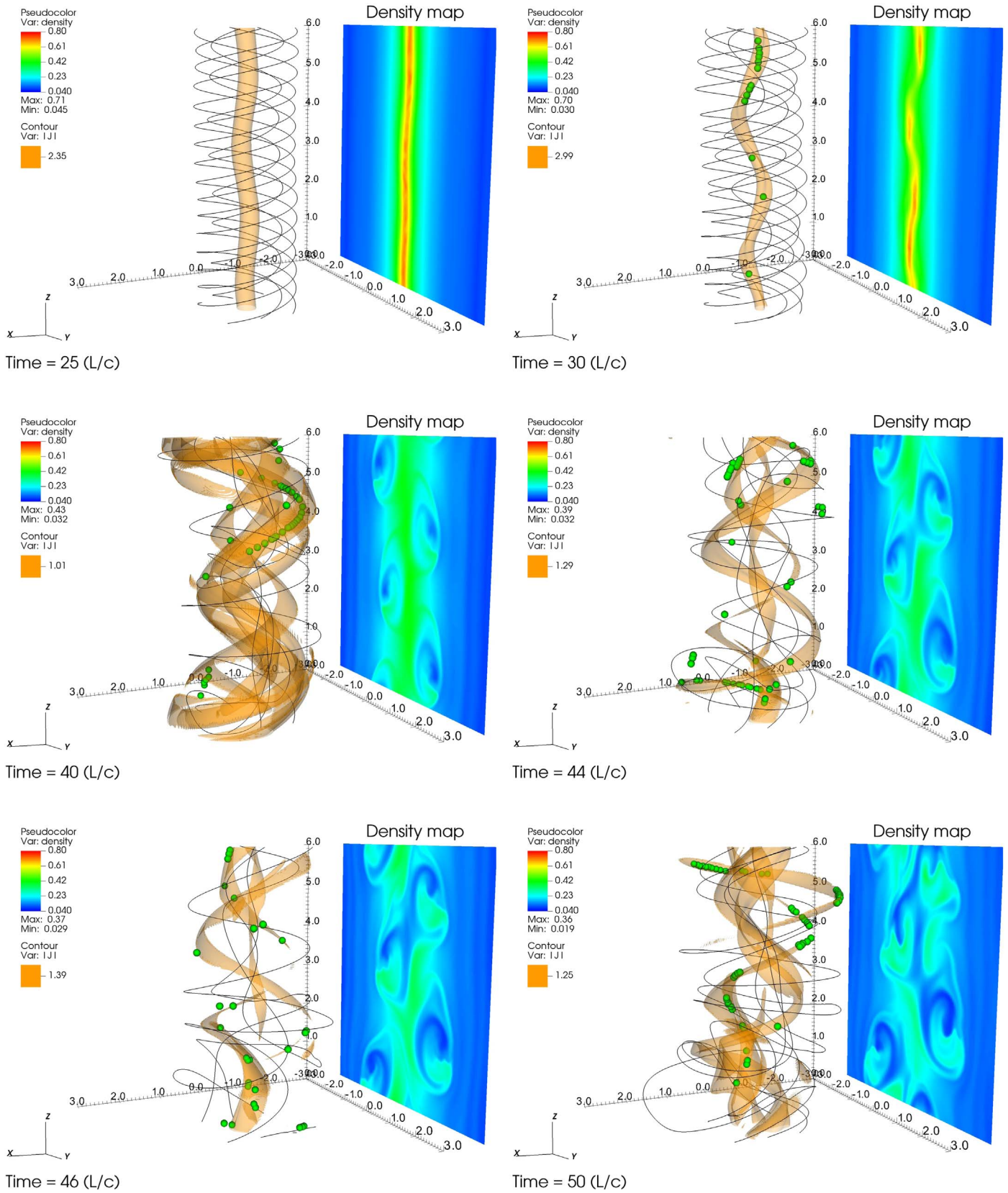

Figure 1. Time evolution of the tower jet at $t = 25$, 30, 40, 44, 46, and 50 L/c (from top left to bottom right). The diagrams depict isosurfaces of the current density intensity at half maximum $|J|$ (orange), the solid black lines correspond to the magnetic field lines, and the green circles correspond to the positions of fast magnetic reconnection regions (with velocities larger than or equal to the average reconnection speed) identified with an algorithm described in Kadowaki et al. (2018b) and KGM20. At the zy plane, we show the density map of the central slice of the jet (at $x = 0$). The time t is in units of L/c, the density is in units of ρ_o, and the current density is in c.u.

Table 3
Reconnection Velocity Values in Units of the Local Alfvén Speed

Jet Snapshot	$\langle V_{\rm rec}\rangle$	$\max(V_{\rm rec})$	Total Counts	Counts ($V_{\rm rec} \geqslant \langle V_{\rm rec}\rangle$)
25	0	0	0	0
30	0.01	0.02	25	11 (44%)
40	0.03	0.06	130	55 (42%)
44	0.03	0.1	161	58 (36%)
46	0.04	0.2	121	39 (32%)
50	0.05	0.1	136	66 (49%)

(see also Kadowaki et al. 2018a; de Gouveia Dal Pino et al. 2018, 2020, and further discussion below).

Figure 2 shows the time evolution of the volume-averaged kinetic energy transverse to the z-axis (Mizuno et al. 2009, 2011, 2012; Singh et al. 2016) within a cylinder of radius $R/L \leqslant 3.0$ around the jet axis,

$$E_{\mathrm{k},xy} = \frac{1}{V_b}\int_{V_b} \frac{\rho v_x^2 + \rho v_y^2}{2} dxdydz, \tag{11}$$

and the volume-averaged total relativistic electromagnetic (EM) energy,

$$E_{\rm em} = \frac{1}{V_b}\int_{V_b} \frac{\boldsymbol{B}^2 + [\boldsymbol{v}^2\boldsymbol{B}^2 - (\boldsymbol{v}\cdot\boldsymbol{B})^2]}{2} dxdydz, \tag{12}$$

where V_b is the total volume where the average is calculated.

As in Mizuno et al. (2012) and Singh et al. (2016), we can use these diagrams to identify the growth of the CDK instability. As it develops, EM energy is converted into kinetic energy, and this is a striking feature revealed by Figure 2. Note that in this figure, the EM energy is presented in linear scale, while the kinetic energy is in log scale. The initial relaxation of the system to equilibrium leads to a hump in the kinetic and EM energy density curves (until $\sim 10\ L/c$).[10] The kink instability comes into play only after the relaxation finishes. There is an initial linear growth of the EM energy between 10 and $\sim 30\ L/c$ due to the increasing wiggling distortion of the magnetic field structure in the jet spine in the initial increase of the CDK instability (which, in log scale, would be harder to perceive; see, e.g., Mizuno et al. 2012). After a slower increase, the kinetic energy undergoes an exponential growth from $t \sim 30\ L/c$ to a maximum near $t \sim 40\ L/c$, after which it approximately reaches a plateau while the magnetic energy decreases (see more details in Singh et al. 2016). We note that this plateau time also coincides with the one after which we have detected an increase in the turbulence and the number of fast reconnection sites in Figure 1. This plateau regime characterizes the achievement of nonlinear saturation of the CDK instability and a nearly steady-state turbulent regime in the system. A similar trend has also been detected in the evolution of the average magnetic reconnection speeds, which nearly achieves a plateau around the same epoch (see Figure 8 in KGM20).

3.2. Particle Acceleration

We have injected test particles into different snapshots of the RMHD jet model j240, specifically in the simulation time

[10] Though the centrifugal and pressure forces of our initial setup are small, they are not entirely negligible; thus, the initial force-free magnetic configuration is not in real equilibrium. Therefore, a little relaxation occurs after a few time steps.

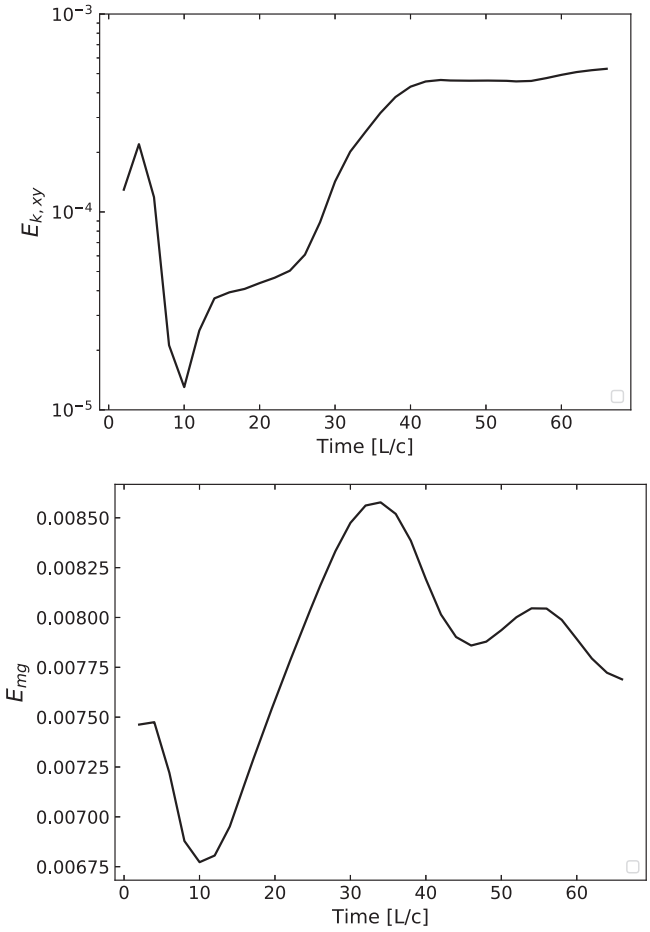

Figure 2. Time evolution of the volume-averaged energy within a cylinder of radius $R/L \leqslant 3.0$ for the simulation. Top: kinetic energy transverse to the z-axis. Bottom: total EM energy. The kinetic energy density is in log scale, while the EM energy density is in linear scale.

$t = 25$, 30, 40, 44, 46, and $50\ L/c$ (see also Figure 1 and Table 2).

Figure 3 shows 2D histograms of the positions of test particles in the snapshots $t = 25$, 30, 44, 46, and $50\ L/c$, projected on planes xy, xz, and yz. All histograms show only the position of particles accelerated with energy increment $\Delta E_p/E_p > 0.4$ (here E_p is the kinetic energy of the proton) and energy larger than 10^2 MeV (or $\sim 10^{-1} m_p c^2$), which is approximately the energy at which it starts an exponential acceleration growth (see Figure 5 in Section 3.2.1). This condition applies to all snapshots except $t = 25\ L/c$, for which particles start to undergo an exponential growth only for energies larger than 10^4 MeV (or $\sim 10 m_p c^2$). Also, only in this snapshot, the particles were injected with a monoenergetic spectrum ($\sim 10 m_p c^2$), as discussed in Section 3.2.2, while in the other snapshots, particles were launched with a Maxwellian distribution (Section 2.2).

When compared to Figure 1, Figure 3 indicates that particles are mainly accelerated along the wiggling jet spine for which the amplitude of the distortion increases as the CDK instability grows, and turbulent disruption develops along with the appearance of fast reconnection regions. Particles are clearly accelerated in these regions where the strength of the current density is larger, and, particularly for times larger than $t = 40\ L/c$, there are clearly several reconnection sites all over the

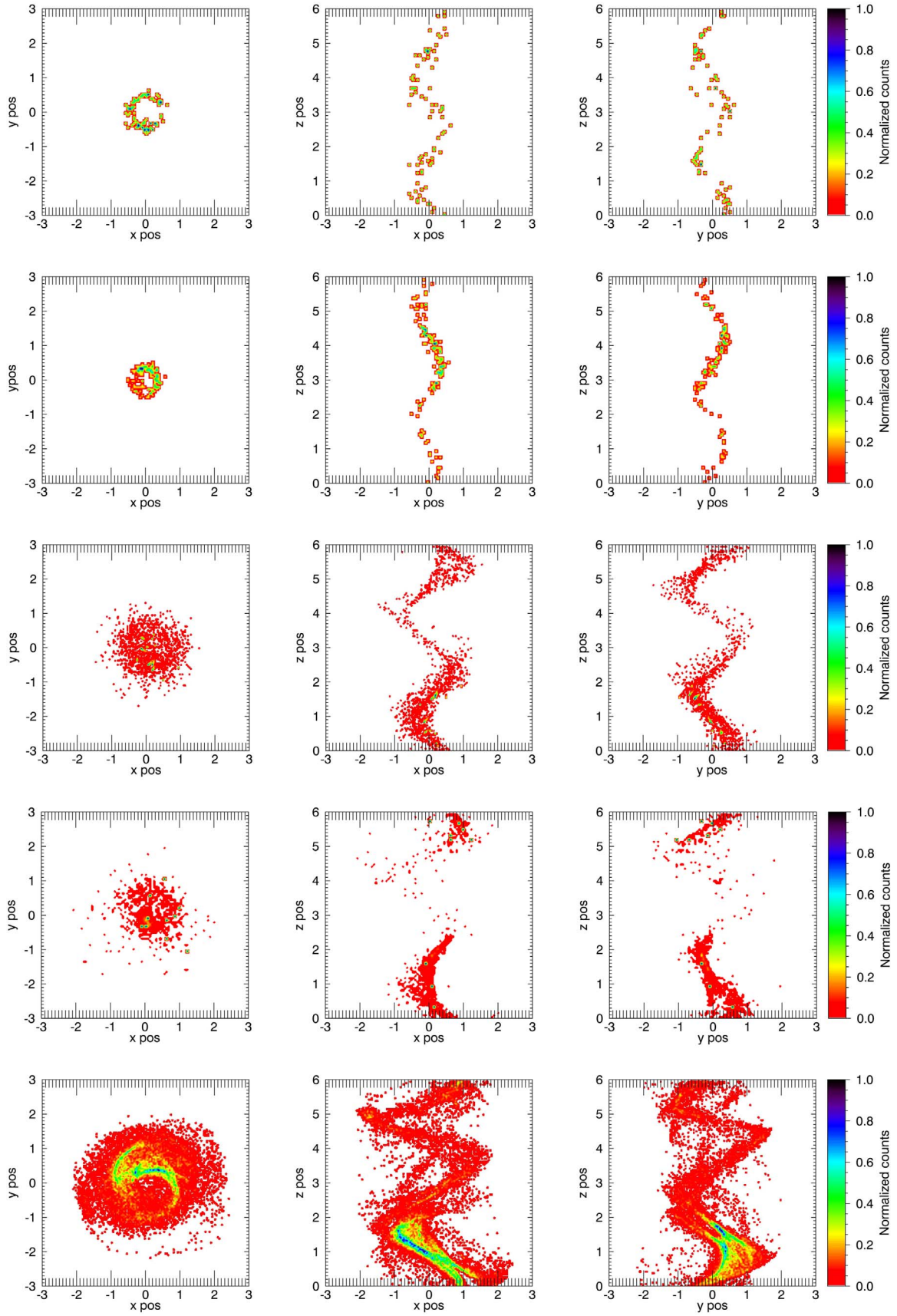

Figure 3. The 2D histograms of particle positions for different snapshots of the model j240. From top to bottom, $t = 25\ L/c$ ($ut25o$), $30\ L/c$ ($t30o$), $44\ L/c$ ($t44o$), $46\ L/c$ ($t46o$), and $50\ L/c$ ($t50o$). Each row shows, from left to right, histograms projected on the xy, xz, and yz planes. To make visualization more clear, the histograms depict only particles accelerating with increment $\Delta E_p/E_p > 0.4$ and energies larger than 10^2 MeV ($\sim 10^{-1} m_p c^2$), except for $t = 25\ L/c$, for which the minimum energy depicted is 10^4 MeV. The different colors indicate the (normalized) concentration of particles in each region of the jet (see text for details).

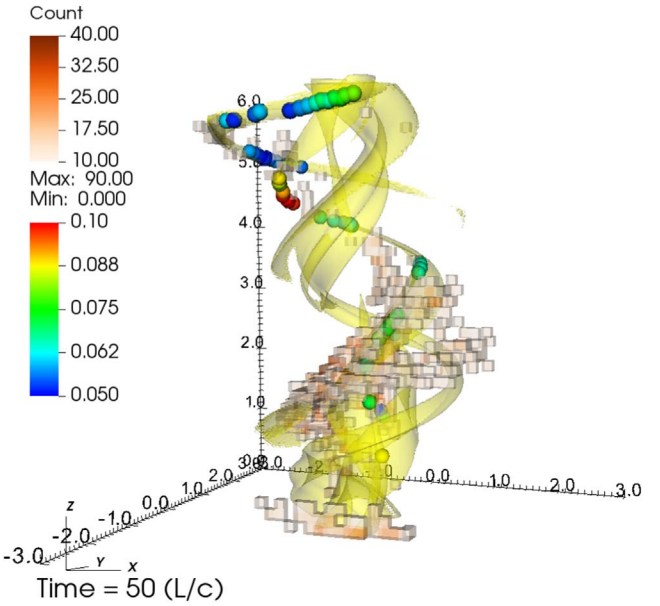

Figure 4. The 3D histogram of accelerated particle positions (squares) for the snapshot $t = 50\,L/c$ of jet model j240. It was integrated over the particles' acceleration time between 100 and 5000 hr, which corresponds to the exponential acceleration regime (see Figure 5, bottom panel). Only the positions of particles accelerated with energy range $[10^{-1}, 10^{7}]m_pc^2$ and energy increment $\Delta E_p/E_p > 0.4$ were included. In order to improve visualization, particles that accelerated to a maximum energy of less than 10^3 MeV were also removed, and to avoid boundary effects, the counts were constrained to the domain range $[-2.5, 2.5]\,L$ in the x and y directions and $[0.5, 5.5]\,L$ in the z direction. The circles correspond to the positions of fast magnetic reconnection sites (with velocities larger than or equal to the average reconnection speed). The isosurfaces of the current density intensity at half maximum $|J|$ (yellow) are also depicted ($J_{\max}/2 \sim 1.25$).

wiggling structure. Note that while the CDK instability is still growing in the early times, in $t = 25\ L/c$, there are no reconnection regions, and in $t = 30\ L/c$, there are only a very few along the jet axis. Particle acceleration in these snapshots will be discussed in Section 3.2.2.

Figure 4 further elucidates these connections between particle acceleration and the sites of high current density and fast reconnection. It depicts a 3D histogram of the accelerated particles for the jet snapshot $t = 50\,L/c$. The histogram was integrated over the particle acceleration time interval between 100 and 5000 hr, which corresponds to the exponential acceleration regime (see Figure 5 and Section 3.2.1 below). As in Figure 3, only the position of particles accelerated with energy increment $\Delta E_p/E_p > 0.4$ and starting with energy $\sim 10^{-1} m_p c^2$ ($\sim$100 MeV) were included. The particles depicted are accelerated up to the saturation energy of the exponential regime, $\sim 10^{7} m_p c^2$ (Figure 5, bottom panel). Figure 4 indicates a clear association of the particles (orange squares) with the acceleration regions, being mostly confined within the wiggling configuration of the half-maximum current density isocontours along the jet spine (shown in yellow). We also see a trend of a larger concentration of particles in regions of faster reconnection rates (green, yellow, and red circles), particularly in the heights between 1.0 and 3.5 L and 4.0 and 5.5 L, approximately. Besides, we note that there are also accelerated particles in the bottom of the domain. Since we have periodic boundary conditions in the z direction, these particles are likely associated with the reconnection sites seen at the top of the

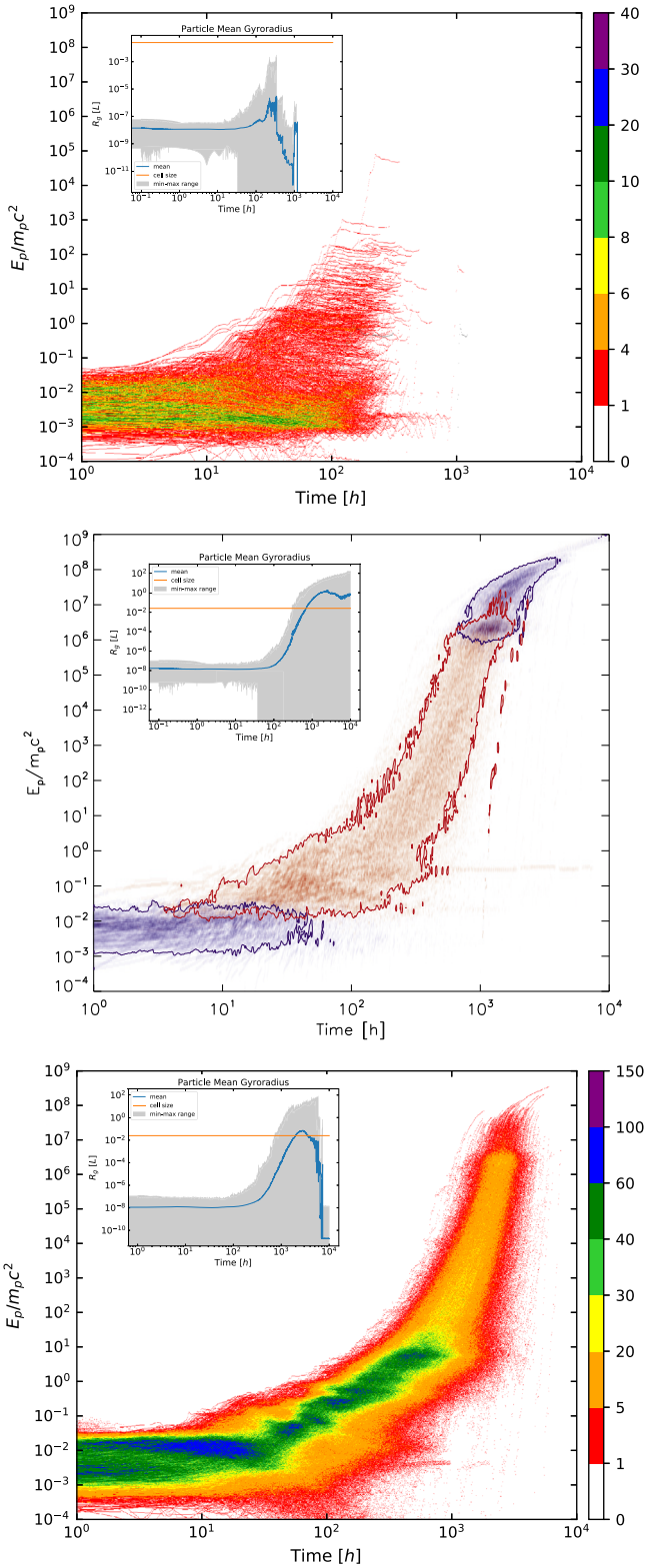

Figure 5. Kinetic energy evolution, normalized by the proton rest mass energy, for the particles injected into the snapshots $t = 40$, 46, and $50\,L/c$ of the jet model j240 (top to bottom). The color bars indicate the number of particles. In the middle panel, the colors indicate which velocity component is being accelerated (red or blue for the parallel or perpendicular component to the local magnetic field, respectively). The insets in the upper left corner of each panel show the time evolution of the particle gyroradius. The horizontal orange line corresponds to the cell size of the simulated background jet, the gray shading corresponds to the entire distribution of gyroradius values, and the blue line gives the average value.

diagram. Finally, there are a few particles at the right edge around height 2.0 L which seem to be detached from the maximum current density layers. An analysis of their energies indicates that most of them have already achieved the saturation value and thus disconnected from the reconnection regions.

In the next paragraphs, we describe in detail the properties and nature of the acceleration of the particles.

3.2.1. Magnetic Reconnection Acceleration

Let us first discuss in detail particle acceleration in the more evolved snapshots of the jet after the CDK instability reaches the plateau, driving fully developed, near steady-state turbulence and fast reconnection all over the jet. Figure 5 compares the kinetic energy evolution of test particles injected into the snapshots $t = 40$ (the initial time of the plateau), 46, and 50 L/c. The inset in each panel shows the evolution of the Larmor radius of the particles, with the orange line representing the cell size of the jet simulation.

As in previous studies of test particles in single current sheets (Kowal et al. 2011, 2012; del Valle et al. 2016), we clearly see that the injected particles, after an initial slow drift, undergo an exponential growth in their kinetic energy up to a maximum value around $\sim 10^7 m_p c^2$ or $\sim 10^{10}$ MeV, around $t \sim 10^3$ hr, for the snapshots $t = 46$ and 50 L/c. This is due to the stochastic Fermi-like acceleration in the current sheets, as described in Section 1 (see also de Gouveia Dal Pino & Lazarian 2005; de Gouveia Dal Pino & Kowal 2015). The maximum energy growth corresponds to a Larmor radius $E/(qB) \sim 4L$, which is approximately equal to the jet diameter, above which the particles escape from the acceleration region (Kowal et al. 2012; del Valle et al. 2016). Beyond this value, the particles' energy may grow still further, as we see for the $t = 46$ and 50 L/c snapshots, but at a smaller rate. As is also seen in Kowal et al. (2011, 2012), this is due to further linear drift acceleration in the varying background large-scale magnetic field of the system. The Larmor radius evolution plots indicate that it is initially very small compared to the size of the cell. When it approaches the cell size, particles then start to interact resonantly with the magnetic fluctuations of the background plasma, undergoing exponential growth in both energy and Larmor radius.

In the snapshot $t = 46$ L/c in the middle panel of Figure 5, we depict which component of the velocity of the particles is being predominantly accelerated (red for the parallel and blue for the perpendicular component to the direction of the local magnetic field). We note that in the exponential regime, there is a clear dominance of the parallel component, characterizing an effective electric field mostly parallel to the reconnection layers, as expected, though the stochastic nature of the whole process also allows for the acceleration of the perpendicular component (see also Kowal et al. 2012). The slower drift acceleration regimes, both in the beginning and after the exponential growth regime, are dominated by the acceleration in the vertical direction. The same behavior has been identified in the other snapshots.

We note that in the snapshot $t = 40$ L/c, which has not yet developed full turbulence with a substantial number of very fast reconnection events (Figure 1 and Table 3), though the particles also undergo exponential acceleration, most of them do not achieve the saturation energy, contrary to what happens in the more evolved snapshots, where nearly steady-state and fully developed turbulence has already been achieved.

3.2.2. Particle Acceleration in the Earlier Stages of the CDK Instability

As remarked previously, there are no reconnection events in the jet snapshot $t = 25$ L/c (Figure 1); thus, one would not expect any acceleration by magnetic reconnection. Nevertheless, motivated by the recent work of Alves et al. (2018), who claimed to detect magnetic curvature drift acceleration in a relativistic jet subject to the kink mode instability, we have also launched test particles in this snapshot in order to seek out this process. The results are presented in Figure 6. The top panel shows particles launched with a similar initial energy distribution and intensity as in the evolved snapshots of Figure 5 (see test particle model *t25o* in Table 2). In this case, we see that some of the particles undergo some acceleration but saturate at an energy $E_p \sim m_p c^2$, which is much smaller than the values reached by the particles accelerated by reconnection in the evolved snapshots of Figure 5. Some particles even lose their energy. On the other hand, if we inject particles with an initially much larger energy, 10^4 MeV or $\sim 10 m_p c^2$ (see test particle model *ut25o* in Table 2), they are accelerated as efficiently as in the evolved snapshots of Figure 5, though we find that some of the particles still lose their energy as in the run of the top panel of Figure 6. A closer view of the plot of the Larmor radius evolution indicates that this also increases exponentially once the value gets closer to the cell size of the background jet and exceeds it. This exponential acceleration is similar to what Alves et al. (2018) obtained in their PIC simulation of a tower jet.

Particle acceleration by magnetic curvature drift may also occur in helical jets subject to kink mode instability (Alves et al. 2018). It may happen in the early stages of the development of the instability, before turbulence and reconnection break out. As we have seen, the kink instability induces a growing helical modulation of the jet spine (see top panels of Figure 1), and the transverse motions excite an inductive electric field, $\boldsymbol{E} = -\boldsymbol{v} \times \boldsymbol{B}$. According to Alves et al. (2018), the axial component of this field $\langle E_z \rangle$ becomes strong and coherent throughout the jet spine when the transverse displacements excited by the tangling magnetic field of the jet become comparable to its radius, i.e., when the kink instability enters the nonlinear regime. This leads to a potent acceleration that we see in the bottom panel of Figure 6. However, we clearly see the difference from the comparison of the two diagrams of Figure 6 that, in order for the particles to obtain the effects of curvature drift, they require some preacceleration.

The bottom panel of Figure 6 also depicts which component of the velocity of the particles is being accelerated (red for the parallel and blue for the perpendicular component to the direction of the local magnetic field). In contrast to the middle panel of Figure 5, we see a dominance of the perpendicular component in the exponential regime and beyond, thus confirming the dominance of the curvature drift acceleration in this case.

Figure 7 depicts the kinetic energy evolution of test particles injected into the jet snapshot $t = 30$ L/c (*t30o* in Table 2), for which a few fast reconnection sites have been detected (see Figure 1). This snapshot is also still in the nonlinear growing phase of the CDK instability in the jet before saturation

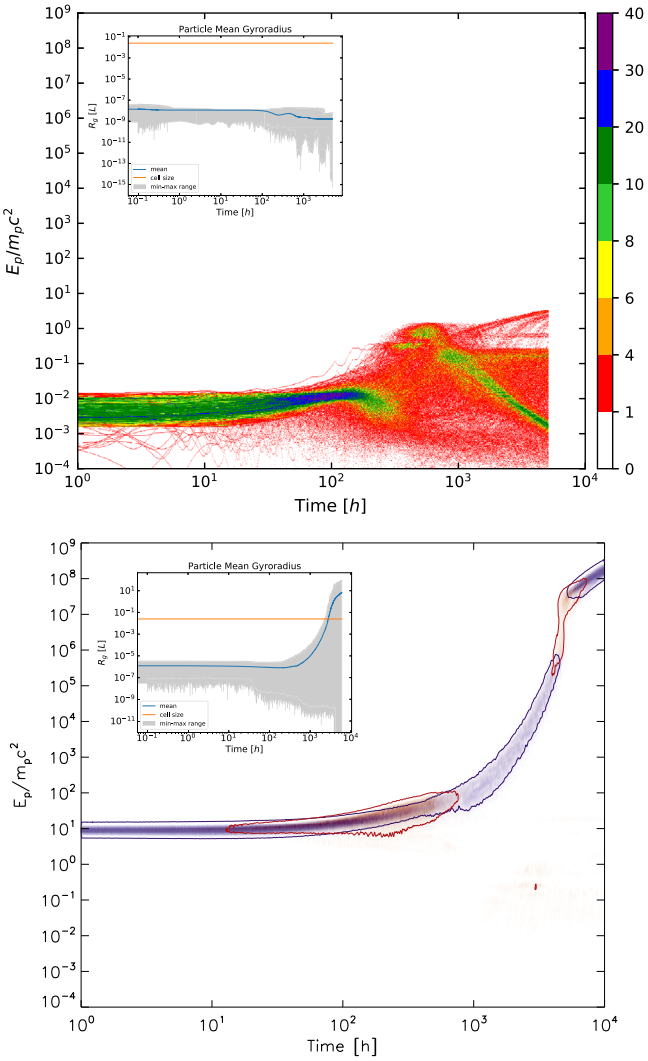

Figure 6. Kinetic energy evolution for particles injected into the snapshot $t = 25\ L/c$ of the jet model j240. The top panel corresponds to particles injected with a Maxwellian distribution and $\langle E_p \rangle \sim 10^{-3} m_p c^2$, as in Figure 5. The color bar indicates the number of particles. The bottom panel corresponds to particles injected with a monoenergetic distribution with larger energy, $E_p \sim 10 m_p c^2$. The colors in this diagram indicate which velocity component of the particles is being accelerated (red or blue for the parallel or perpendicular component to the local magnetic field, respectively). The insets depict the evolution of the particle gyroradius, same as in Figure 5.

(Figure 2). The particles were injected with the same initial energy ~1 MeV ($\sim 10^{-3} m_p c^2$) as in the evolved jet snapshots of Figure 5 or the model of the top panel of Figure 6.

Interestingly, the particles now undergo an exponential increase in kinetic energy up to the same maximum value of the more evolved snapshots (Figure 5, snapshots $t = 46$ and $50\ L/c$), even having only a few fast reconnection sites. Furthermore, contrary to what we see in snapshot $t = 25\ L/c$ (Figure 6), where particles could accelerate by magnetic curvature drift only starting with injection energy around 10^4 MeV (or $\sim 10 m_p c^2$), at $t = 30\ L/c$, they get accelerated starting with energies well below $\sim 10^{-3} m_p c^2$, as in the evolved snapshots. These results suggest that the particles are also experiencing magnetic reconnection acceleration in this case. Moreover, it seems that when reconnection is present, particles do not require preacceleration, as in the $t = 25\ L/c$ snapshot

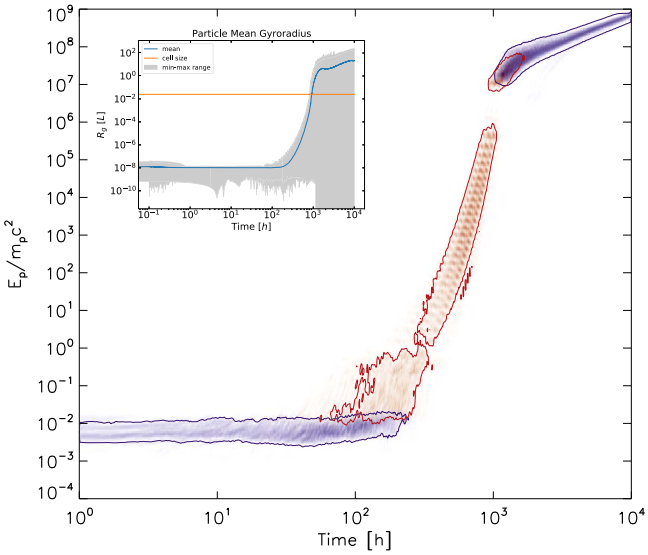

Figure 7. Kinetic energy evolution for particles injected into the snapshot $t = 30\ L/c$ of the jet model j240. As in Figure 5, particles are injected with $\langle E_p \rangle \sim 10^{-3} m_p c^2$ and a Maxwellian distribution. The colors indicate which velocity component of the particles is being accelerated (red or blue for the parallel or perpendicular component to the local magnetic field, respectively). The inset depicts the evolution of the particle gyroradius.

(Figure 6, bottom panel). During the exponential growth, due to the fact that both processes, i.e., fast reconnection and a large-amplitude tangled spine with a still coherent magnetic field, are present, it is possible that both mechanisms, curvature drift and reconnection acceleration, are operating simultaneously. This combination may also explain why we see a more efficient acceleration in this snapshot than around $t = 40\ L/c$, when the CDK instability had just saturated and the turbulent reconnection driven by it had just broken out.

In fact, Figure 7 indicates that the dominant velocity component accelerated in the exponential region is the parallel (as in Figure 5, middle panel), though the number of particles is smaller in this regime, while in the more extended region of slower acceleration beyond that, where we see a much larger concentration of particles, the dominant component is the perpendicular one. The dominance of the parallel component in the exponential region is suggestive of a predominance of reconnection acceleration, while the dominance of the perpendicular component in the second region is characteristic of curvature and normal drift acceleration.

3.2.3. Resolution Effects

In order to examine potential resolution effects, we have also injected test particles into a higher-resolution background relativistic jet simulation (model j480 of Table 1). Figure 8 shows the kinetic energy evolution for accelerated particles launched at snapshot $t = 50\ L/c$ of this jet (test particle model 480t50o in Table 2). The initial conditions for this run are the same as in the corresponding lower-resolution model at $t = 50\ L/c$ (see bottom panel of Figure 5).

Comparing Figure 8 with its lower-resolution counterpart in Figure 5 (bottom panel), we clearly see that they are very similar. The only visible difference is due to the number of test particles used in each test. In the snapshot of the lower-resolution jet model, we employed 10,000 particles, while in the high-resolution jet model, we injected only 1000 particles for being computationally much more time-consuming and

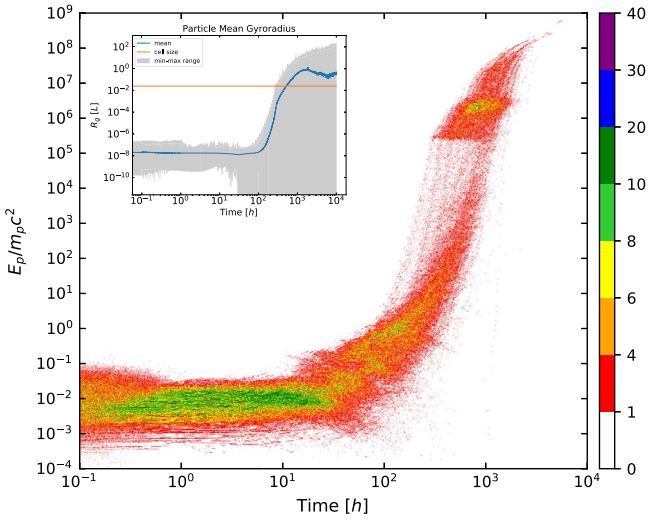

Figure 8. Particle kinetic energy evolution, normalized by the rest mass energy, for 1000 protons injected into the $t = 50\,L/c$ snapshot of the higher-resolution jet model (t480; see Table 1). The initial conditions for the test particles are the same as in the lower-resolution test shown in Figure 5 for the same time step (bottom panel), except that 10,000 protons were used there. The color bar indicates the number of particles. The inset shows the evolution of the particle gyroradius.

expensive. The energy growth rate is also very similar in both cases, as we will see in the next section (Figure 9), though the particles in the higher-resolution case reach the saturation energy of the exponential growth regime a little before 10^3 hr, while in the low-resolution jet, it is a little after 10^3 hr, reflecting a slightly larger acceleration rate in the higher-resolution case (see Figure 9).

This is due to the fact that in the higher-resolution jet (smaller cell size), more regions of fast magnetic reconnection can be resolved at smaller scales, so that particles, starting with a smaller Larmor radius, can interact more frequently with resonant magnetic fluctuations, making the acceleration rate slightly more efficient. In fact, we have found that the number of reconnection sites is six times larger than in the lower-resolution jet. Nevertheless, since the change in the acceleration rates or particle spectra are not substantial (see Sections 3.2.4 and 3.2.5), we proceed with our analysis considering the lower-resolution jet model (j240) because the employment of the larger-resolution counterpart for the entire analysis would be computationally rather long and expensive.

We should note that we have also repeated the test particle run for the snapshot $t = 25\,L/c$ (as in the top panel of Figure 6, Section 3.2.2) but employing the higher-resolution jet model (j480), and we have obtained the same result, thus showing that that result is also not changed by the increase of the background resolution.

3.2.4. Particle Acceleration Rates

Magnetic reconnection acceleration, as in the Fermi process, predicts a dependence of the acceleration rate with the reconnection velocity and particle energy (de Gouveia Dal Pino & Kowal 2015; del Valle et al. 2016; Matthews et al. 2020). Similar to del Valle et al. (2016), in order to quantify the effectiveness of the acceleration of the particles for each test particle model (Table 2), we have calculated the average time per energy interval that particles take to reach a certain energy, which gives the acceleration time as a function of the energy

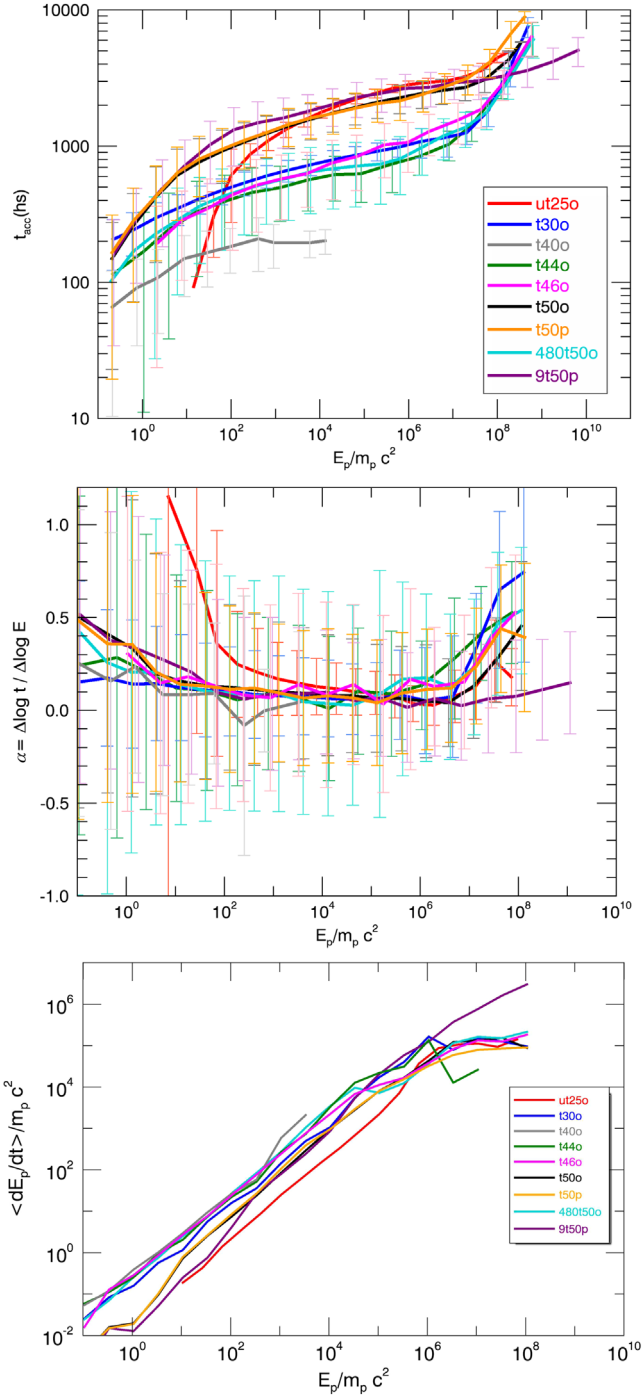

Figure 9. Acceleration time (top panel), power-law index of the acceleration time α index (middle), and kinetic energy growth rate (bottom) as functions of the particle kinetic energy normalized by the proton rest mass energy for the different test particle models of Table 2. The error bars are obtained by calculating the standard deviation.

shown in Figure 9 (top panel) for all models. Using the same simulated data set, we depict in Figure 9 (middle panel) the power-law index, $\alpha = \Delta\log(t_{\rm acc})/\Delta\log E_p$, of the acceleration time dependence with particle energy, $t_{\rm acc} \propto {E_p}^{\alpha}$.

In the top and middle panels of Figure 9, the particles in the different models enter the exponential growth regime of acceleration approximately around the energy $\sim 10^{-1} m_p c^2$ (in agreement with the diagrams of kinetic energy evolution of Figures 5–8) and end the exponential growth near $\sim 10^{7} m_p c^2$

(except for model $9t50p$, which we discuss below in Section 3.2.7). Before starting the exponential acceleration, the particles experience slower growth in their energies, which is reflected in the larger α index, especially for $t = 25\ L/c$. The test corresponding to the snapshot $t = 30\ L/c$ has the smallest α during this initial phase (dark blue line in Figure 9), characterizing a smoother transition to the exponential acceleration regime. This is compatible with the previous analysis, where we saw that in this early snapshot, the particles are experiencing both magnetic curvature drift and reconnection acceleration. During the exponential growth regime, α decreases to similar values around $\alpha \sim 0.09 \pm 0.05$ for all models and energies in this regime.[11]

Beyond the exponential regime, the acceleration time and α index grow a little further due to the slower drift acceleration that particles experience after leaving the reconnection (or curvature drift, in the case of $t = 25\ L/c$ acceleration regions, as discussed in Figures 5–8 and Sections 3.2.1 and 3.2.2).

The kinetic energy growth rate as a function of the particle energy depicted in the bottom panel reflects the results of the top panel. It increases with the energy at the same rate in the exponential regime for all models. Interestingly, the only model that shows a slightly smaller rate (and slightly larger α index) is the one corresponding to snapshot $t = 25\ L/c$, possibly due to the different acceleration process.

A closer look at the acceleration time presented in the top panel of Figure 9 shows some slight differences between the models. Though these differences are approximately encompassed by the uncertainties of the numerical calculations (as we see from the error bars, which were calculated by the standard deviation method), the higher-resolution jet model ($480t50o$) produces a slightly smaller acceleration time than its lower-resolution test counterpart ($t50o$). This is compatible with the results found in Figures 5 and 8 (bottom), discussed in Section 3.2.3.

Another interesting result is that for snapshot $t = 30\ L/c$ ($t30o$ in Figure 7), which also shows a smaller acceleration time comparable to that of more evolved snapshots, like $t = 44\ L/c$ ($t44o$) and $t = 46\ L/c$ ($t46o$), for which we have detected a large number of fast reconnection sites with rates larger than the average value (see Table 3). Furthermore, these tests have acceleration times comparable to the high-resolution model ($480t50o$). Regarding the models $t44o$ and $t46o$, the larger efficiency can be attributed to the larger number of fast reconnection regions, while in $t30o$, this seems to be due to the combination of the two acceleration processes (as discussed in Section 3.2.2).

More peculiar behavior is found in the acceleration time for the snapshot $t = 40\ L/c$ ($t40o$ in the top panel), which shows the lowest values since the beginning. We recall that this snapshot corresponds to the plateau of the CDK instability and the transition of the jet from the laminar to the fully developed turbulence regime. Besides, it already has several sites of fast reconnection, but all have velocities near the average value (Figure 1 and Table 3). Moreover, Figure 5 (top) indicates that in this snapshot, most of the particles enter the exponential regime of acceleration but do not achieve the saturation energy. All of these facts combined seem to have favored this slightly smaller acceleration time in the beginning of the acceleration for this snapshot in the transition regime.

[11] We note that the error in this determination was derived by taking into account only the models having the jet j240 as background, but the same value of α is derived for the particle models having the higher-resolution jet as background.

3.2.5. Particle Spectrum

Figure 10 shows the evolution of the energy spectrum of all particles (not only the accelerated ones) during the acceleration in the jet snapshots at $t = 25\ L/c$ (particle model $ut25o$), 30 ($t30o$), 46 ($t46o$), and $50\ L/c$ ($t50o$; top to bottom). Several time intervals are depicted in each panel in units of hours. Initially, the particles have a Maxwellian distribution (red line), except in the top panel for the jet snapshot $t = 25\ L/c$, where the injection spectrum is monoenergetic (with $\sim 10 m_p c^2$). As particles accelerate, they start to populate the higher-energy tail of the distribution, which becomes flatter at these energies (see third and fourth panels, in particular). We should remember that in our numerical setup, particles are continuously reinjected into the system; therefore, they never stop being accelerated. For this reason, the distribution shifts to larger and larger energies. Furthermore, even after the particles attain the maximum (saturated) energy at the end of the exponential acceleration regime due to reconnection (or magnetic curvature in the case of the snapshot $t = 25\ L/c$; top panel), they continue to accelerate at a smaller rate due to normal drift (as remarked in Section 3.2.1).

We should also remember that the maximum energy achievable by the stochastic mechanism (at the saturation of the fast acceleration growth) occurs around $t \sim 10^3$ hr for all models depicted (see Figures 5 and 6), except the top one, for which this occurs around $t \sim 10^{3.5}$ hr (see Figure 6). Interestingly, we see that for this model ($ut25o$) and model $t30o$ (second pane), around these times, there is a double hump in the distribution (green dotted–dashed curve), with an accumulation of particles at energies above $10^7\ m_p c^2$ for both, thus highlighting the transition from the exponential to the linear drift acceleration regimes. In the other models depicted, this transition is more smooth. Also notable is the double peak in the distribution that appears in model $t30o$ in earlier times at $t \sim 10^2$–$10^{2.3}$ hr. This is possibly connected to the superposition of the two acceleration processes in this model, namely the magnetic curvature drift and the reconnection acceleration, as we discussed in Section 3.2.2.

Perhaps the most striking feature in all of the diagrams of Figure 10 is that as particles reach VHEs, the distribution may even attain an almost zero power-law index tail in very evolved times, as we clearly see in the bottom panel of the figure. In real systems, however, this acceleration process should be interrupted by the escape of the particles from the finite volume of the acceleration zone and also due to radiative losses. As stressed above, since in our simulations, the particles are continuously accelerated and there is no physical mechanism to allow them to escape, it is not possible to obtain the actual distribution of the accelerated particles. However, we can at least estimate the power-law index of the distribution soon after the particles start to populate the high-energy tail (see, e.g., del Valle et al. 2016).

In Figure 11, we show the total number of particles as a function of energy for two different early time steps of the acceleration for the jet snapshot $t = 50\ L/c$. The initial Maxwellian (normal) distribution is shown with a gray dotted line. The earliest time step plotted corresponds to the approximate time when a high-energy power-law tail starts to form (i.e., when particles reach kinetic energies larger than

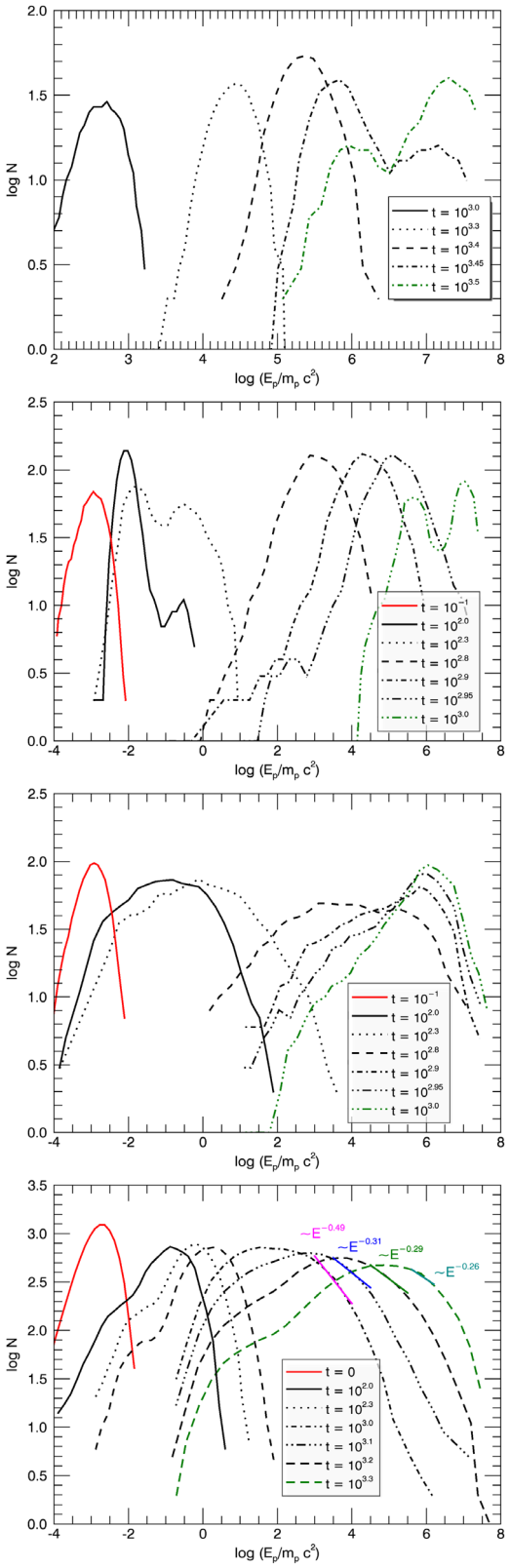

Figure 10. Particle energy spectrum evolution as a function of the normalized kinetic energy ($m_p c^2$) in the jet snapshots, from top to bottom: $t = 25$ (particle model *ut*25*o*), 30 (particle model *t*30*o*), 46 (*t*46*o*), and 50 L/c (test particle model *t*50*o*). The red line in all panels but the top corresponds to the initial Maxwellian distribution of the particles. In the top panel, particles are injected with a monoenergetic spectrum. The time steps (in hours) of the acceleration are depicted in the detail of each panel.

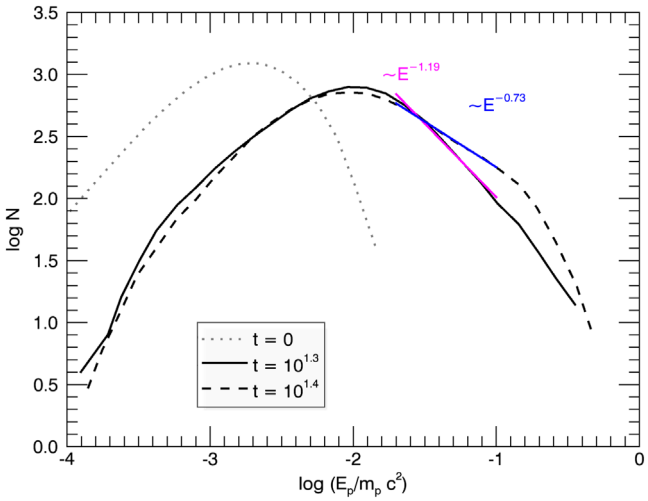

Figure 11. Particle energy spectrum as a function of the normalized kinetic energy at two different early time steps of the acceleration (in hours) for the jet snapshot $t = 50\,L/c$. The gray dotted line is the initial Maxwellian distribution. The high-energy tail of each distribution is fitted by a power law.

$\sim 10^{-1}\, m_p c^2$, according to Figure 5, bottom panel); the second time corresponds to a little later time step. We see that the power-law index at the earlier time can be fitted by $p = -1.19$. The second power law at a later time is flatter due to the effects discussed above; therefore, it must only be taken as illustrative of the limitations of the method. Of course, in realistic systems, the presence of physical particle escape from the acceleration zone, radiative losses, and dynamical feedback of the accelerated particles into the plasma will result in a steeper spectrum in the late times too ($|p| > 1$).

3.2.6. Boundary Effects

As described in Section 2.2, in most of the particle runs, we have allowed the particles to reenter the system only through the jet periodic boundaries along the z direction. Nevertheless, we have also performed a few tests where we allowed the particles to be reinjected into the system through all of the boundaries, i.e., also when crossing the jet outflow boundaries in the x and y directions, aiming at increasing the number of accelerated particles. In Table 2, these few tests are labeled with a "p." Figure 12 shows one of these tests performed for the jet model j240 in the snapshot $t = 50\ L/c$ (model *t*50*p*), for which 1000 particles were initially injected. It can be compared with its counterpart model shown in the bottom panel of Figure 5, in which 10,000 particles (rather than 1000) were injected and allowed to reenter the system only in the z direction (test particle model *t*50*o*; Table 2). We note that both models have very similar behavior, except for the number of particles that are being accelerated along the system evolution. While in model *t*50*o* (bottom panel of Figure 5), there are more particles in the beginning of the evolution due to the much larger number of injected particles, in model *t*50*p* (Figure 12), we see a larger number of particles that are accelerated up to the maximum energy at the exponential regime and beyond due to the larger number of reinjected particles in the periodic boundaries in all directions. We also see in Figure 9 that both models have similar acceleration properties, i.e., acceleration rate, power-law index α, and kinetic energy growth rate.

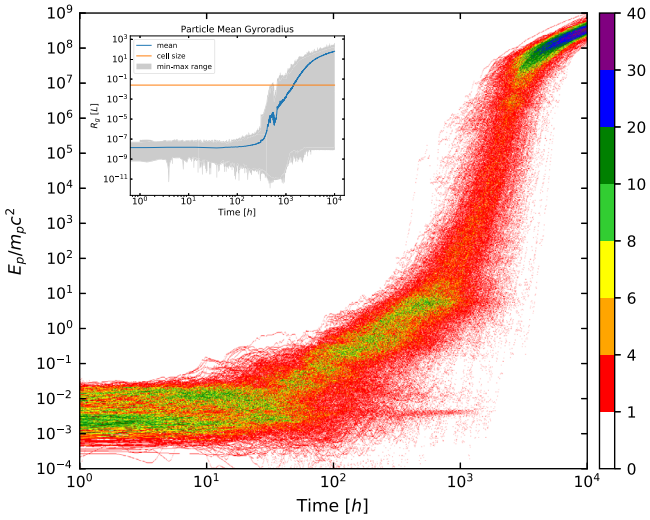

Figure 12. Particle kinetic energy evolution, normalized by the rest mass energy, for particles injected into the $t = 50\,L/c$ snapshot of the jet model (j240; see Table 2). This test is similar to that of the bottom panel of Figure 5, except that here particles were periodically reinjected through all of the boundaries of the jet system (see model $t50p$ in Table 2). The color bar indicates the number of particles. The inset shows the evolution of the particle gyroradius.

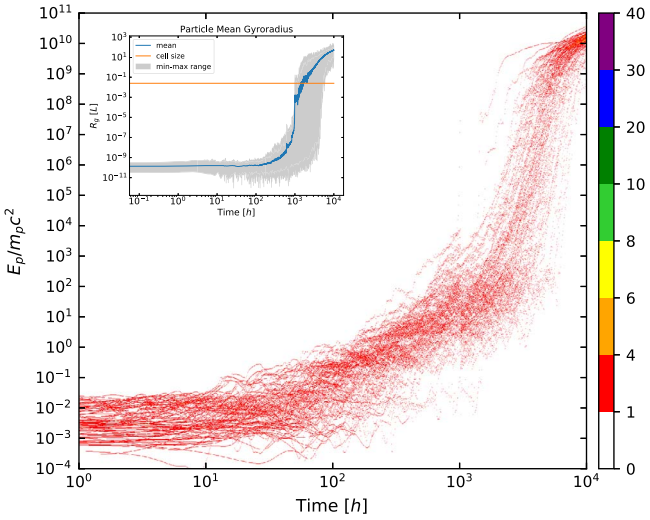

Figure 13. Kinetic energy evolution for particles injected at snapshot $t = 50\,L/c$ of the jet model j240 with an initial background magnetic field at jet axis $B_0 = 9.4$ G and a background density $\rho_0 = 10^4$ cm^{-3} (see Table 2). The initial conditions are the same as in the test particle model ($t50o$) shown in the bottom panel of Figure 5, except that there, $B_0 = 0.094$ G and $\rho_0 = 1$ cm^{-3}, leaving the Alfvén velocity unaltered in both tests (see text for details). The color bar indicates the number of particles, and the inset shows the evolution of the particle gyroradius.

3.2.7. Magnetic Field Effects

As in Figure 5 (bottom diagram, test particle model $t50o$), Figure 13 also shows the kinetic energy evolution for particles injected at snapshot $t = 50\ L/c$ of the jet model j240, except that now the initial background magnetic field at the jet axis is 100 times larger ($B_0 = 9.4$G), corresponding to the test particle model $9t50p$ of Table 2.[12] This change in the physical unit value of the magnetic field of the background jet was made in such a way that we have kept the scale invariance in the jet system. In other words, as stressed in Section 2, the magnetic field c.u. in the RMHD jet simulation is given by $\sqrt{4\pi\rho_0 c^2}$. Thus, when increasing the physical unit of the magnetic field by a factor of 100, we also had to increase the background density physical unit by a factor of 10^4 in order to keep the magnetic field in c.u. unaltered and thus the corresponding Alfvén speed. This means that in this test particle model with larger physical magnetic fields and densities ($9t50$), the background reconnection velocities have also been the same as in model $t50o$. Therefore, the particles in this new model ($9t50$) should feel essentially the same acceleration rates of the counterpart test model with a smaller jet magnetic field and density (model $t50o$). This is what we see comparing these models in the diagrams of Figure 9.

On the other hand, a closer view of Figure 13 shows that the increase of the background magnetic field by a factor of 100 causes an increase of the maximum energy achieved by the particles by 2 orders of magnitude with respect to the counterpart model $t50o$ (see Figure 5, bottom panel). In other words, while the maximum energy that particles attain in the exponential regime in model t50o is $\sim 10^7 m_p c^2$, in model $9t50$, it is $\sim 10^9 m_p c^2$ (see also Figure 9). The plot in the detail of Figure 13 shows that the corresponding maximum Larmor radius ($\propto E_p/B$) is the same as in model $t50o$; this because in both test particle models, the ratio of the maximum energy to the background magnetic field is the same, or in other words, the physical size of the acceleration region is the same in both cases.

[12] We note that this test particle model $9t50p$ was run with periodic boundaries in all directions, while the counterpart model used for comparison with it, $t50o$ (Figure 13), has periodic boundaries only in the z direction. However, as we have seen in Section 3.2.6, the employment of periodic boundaries in all directions produces results very similar to the corresponding model with periodic boundaries only in the z direction.

4. Discussion and Conclusions

In this work, we have investigated the acceleration of particles injected into several snapshots of a 3D Poynting flux–dominated jet with moderate magnetization ($\sigma \sim 1$) subject to CDK, which drives turbulence and fast magnetic reconnection. Our results can be summarized as follows.

1. Once turbulence driven by the CDK instability is fully developed in the jet, achieving a nearly steady state, the amplitude of the excited wiggles along the jet spine also attains maximum growth and gets disruptive with the formation fast magnetic reconnection in several sites. This occurs after the jet snapshot $t \sim 40\ L/c$, when the CDK instability achieves a plateau. Injecting hundreds to thousands of protons into jet snapshots more evolved than this one, we find that, after about 10^2 hr, the particles undergo an exponential acceleration up to a maximum energy. For a background magnetic field around $B \sim 0.1$ G, this saturated kinetic energy is $\sim 10^7 m_p c^2$, or $\sim 10^{10}$ MeV (Figure 5), while for a magnetic strength 200 times larger, $B \sim 1$ G, the maximum accelerated energy also increases by a factor of 100, to $\sim 10^9 m_p c^2$, or $\sim 10^{12}$ MeV (Figure 13). Beyond these values, the particles suffer further acceleration (to energies up to 100 times larger) but at a much slower rate due to drift in the varying magnetic field.
2. Particles achieving the saturation energy in the exponential regime of acceleration attain a Larmor radius comparable to the size of the acceleration region of $\sim 4L$, which is of the order of the diameter of the

perturbed wiggled jet. This regime of particle acceleration is very similar in all these evolved snapshots, where it lasts for several hundred hours until the particles reach the saturation energy.

3. In a companion work (KGM20), we have quantitatively identified the sites of reconnection over the entire jet, and here we could correlate them with the accelerated particles (Figures 3 and 4). The results show a clear association with the regions of maximum current density and fast reconnection sites, indicating that particles are mostly being accelerated by magnetic reconnection, as detected in previous studies (e.g., Kowal et al. 2011, 2012; del Valle et al. 2016). The exponential acceleration in these sites is suggestive of a Fermi stochastic process (e.g., de Gouveia Dal Pino & Lazarian 2005; Kowal et al. 2011, 2012; de Gouveia Dal Pino & Kowal 2015; Matthews et al. 2020). Furthermore, during the exponential regime, we have found a predominance of acceleration of the parallel component of the particle velocity to the local magnetic field, which is characteristic of acceleration in reconnection domains.
4. In the early stages of the development of the nonlinear growth of the CDK instability, before this achieves the plateau and the magnetic field lines start disruption, the jet spine oscillates with growing amplitude. We find that during this early stage (jet snapshot $t = 25\,L/c$), there are no sites of fast reconnection, but the test particles are efficiently accelerated by magnetic curvature drift, with a dominance of acceleration of the perpendicular component of the particles' velocity to the local magnetic field, similar to what was detected in the PIC simulations of Alves et al. (2018). However, in order for the particles to get accelerated by this process, they had to be injected with an initial energy much larger than that required for the particles to accelerate in the reconnection sites of the jet in later snapshots. While in the more evolved snapshots, particles can be injected with energies 10^{-3} $m_p c^2$ or less, in this early snapshot, they have to be injected with at least 10 $m_p c^2$ to be accelerated (4 orders of magnitude larger). This suggests that this mechanism requires preaccelerated particles in order to work efficiently. This was confirmed by another test, where we injected particles into a later jet snapshot, $t = 30\,L/c$, where the wiggling amplitude of the magnetic field in the jet spine was still coherent but a few sites of fast reconnection had already developed. In such background conditions, we find that the particles undergo an efficient acceleration starting with an injection energy of only $10^{-3} m_p c^2$. This occurs because, in this case, particles are being accelerated from the beginning in the reconnection sites and then further accelerated in the wiggling spine by curvature drift (Figures 6 and 7).
5. The acceleration time due to magnetic reconnection indicates a weak power-law dependence with the particle energy given by $t_A \propto E^{\alpha}$, with $\alpha \sim 0.1$, obtained from all test particle models.
6. The energy spectrum of the accelerated particles develops a high-energy tail that can be fitted by a power-law index $p \sim -1.2$ in the beginning of the acceleration; this does not depend on the initial energy of the injected particles, at least in cases of acceleration by magnetic reconnection.
7. Particles injected into the background jet assuming periodic conditions in all boundaries or periodic boundaries only in the z direction (along the jet axis) and outflow boundaries in the transverse direction produce similar results. The only remarkable difference is that the adoption of periodic boundaries in all directions allows for particles to reenter the system more frequently, thus increasing the number of accelerated particles.

The results above have important implications for particle acceleration and the associated nonthermal emission in relativistic jets, especially in their magnetically dominated regions. Though we have not taken into account particle losses, such as nonthermal radiation, electron–positron pair production, particle back reaction into the jet plasma, or particle diffusion, the energies achieved by the particles, $\sim 10^{16}$ or $\sim 10^{18}$ eV (or even larger), depending on the strength of the background magnetic fields, ~ 0.1 or ~ 10 G, are more than sufficient to explain energetic particles and even ultra-high-energy cosmic rays (UHECRs) in these sources. Protons with these energies could explain observed VHE emission, as well as the production of neutrinos, out of interactions with the ambient photon and density fields in relativistic jets. This could be the case, for instance, of blazars like TXS 0506+056 (Aartsen et al. 2018), for which has been observed for the first time simultaneous TeV gamma rays and neutrino emission. Although there might be other possibilities (see, e.g., Cerruti 2020), this process should be explored in detail elsewhere. In our companion work, KGM20, we have applied the results of this study of magnetic reconnection in jets to the VHE light curve of the blazar Mrk 421 (e.g., Kushwaha et al. 2017) and found that the magnetic power and variability obtained from the reconnection events are compatible with the observed emission.

Our results are comparable to those obtained from test particles injected into single nonrelativistic current sheets in which forced turbulence was introduced to make reconnection fast (e.g., Kowal et al. 2011, 2012; del Valle et al. 2016). Del Valle et al. (2016), for instance, obtained an acceleration time with a similar weak energy dependence, with a power-law index $\alpha \sim 0.2$–0.6 for a vast range of reconnection velocities. The slightly smaller values of α we obtained in this work are consistent with the fact that the jet has relativistic Alfvén velocities and thus intrinsically higher reconnection speeds, $V_{\rm rec} \simeq 0.05 V_A$, that naturally make the process slightly more efficient. In del Valle et al. (2016), the particle spectrum power-law indices derived in the beginning of the acceleration process are also compatible with our results. Moreover, our power-law indices are remarkably similar to those obtained from PIC simulations of single current sheets in the kinetic scales of the plasma (e.g., Zenitani & Hoshino 2001; Drake et al. 2013; Sironi & Spitkovsky 2014; Guo et al. 2014, 2015; Li et al. 2015; Werner et al. 2018).

These results are also consistent with the theoretical models of the Fermi acceleration process in reconnection sites (e.g., de Gouveia Dal Pino & Lazarian 2005; Drury 2012; de Gouveia Dal Pino & Kowal 2015), which predict an acceleration time similar to that of stochastic shock acceleration and approximately independent of the reconnection velocity. Similar to these earlier studies, particles achieve maximum energy when their Larmor radii become comparable to the size of the acceleration zone.

It is important to remark that in this work, we have neglected potential effects of the dynamical variations in the background plasma on the acceleration of the particles. More specifically, we have neglected the betatron effect (see, e.g., Kowal et al. 2012; de Gouveia Dal Pino & Kowal 2015). When performing test particle simulations into an MHD background system, in order to follow the particles' interactions with it, we have to transform the background c.u. to physical units. As we have normalized the particles' time unit in hours, this means that, for instance, from the background snapshot $t = 40\ L/c$ to $t = 50\ L/c$, 10 hr have elapsed. Now, particles interact resonantly with the magnetic background fluctuations (according to Equation (10)) when their Larmor radii are comparable to the wavelength of these fluctuations. When the turbulence in the jet attains a nearly steady-state regime (beyond $t = 40\ L/c$ in the jet), the background dynamical variations become statistically negligible. In other words, the particles face a very similar background spectrum of fluctuations in the reconnection regions spread over the distorted magnetic field spine and outside them in every snapshot of this nearly stationary regime. This is consistent with results we obtain for the particle acceleration properties for the evolved snapshots $t = 46$ and 50 L/c, which are very similar (see Figures 5 and 9). Previous studies of the betatron effect, which performed test particle simulations considering the dynamic variations of the MHD background (between snapshots), have shown that, in the case of pure turbulent environments (i.e., where the reconnection acceleration favors a second-order Fermi over a first-order Fermi, and thus this effect is more important), it introduces only a factor of 2 difference in the acceleration rate (e.g., de Gouveia Dal Pino & Kowal 2015, and references therein). Since particles attain energies that are more than 8 orders of magnitude larger than the energy at injection, this effect is almost negligible. It may have some impact (of a factor of 2) only in the beginning of the acceleration when the particles are still growing their energy linearly, essentially by drift acceleration. We have plans to perform studies of the particle back-reaction in the CDK unstable jet by incorporating particles directly into the RMHD code. This will allow us to both compute the particles' back-reaction in the fluid and perform a more accurate estimation of the betatron effect. With regard to the earlier snapshots ($t = 25$, 30, and 40 L/c), when the CDK instability and the turbulence are still growing and the system has not yet achieved a nearly steady state, one may argue that the background dynamical effects might have implications for the stochastic reconnection acceleration evolution in these cases. However, at $t = 25\ L/c$, the system has no fast reconnection current sheets yet, and the particles experience only magnetic curvature drift acceleration, as discussed in Section 3.2.2. Of course, this ideal situation may not be sustained for long in the real jet, since the CDK instability grows fast, but it illustrates what may happen with particles in the early stages of the growth of the instability and also serves to compare with other (PIC) works (e.g., Alves et al. 2018; see below). The snapshot 30 L/c, on the other hand, already has a few fast reconnection sites, and, as discussed in Section 3.2.2, it combines the two processes of acceleration. The inclusion of the dynamical effects of the background in this case would not affect the results much, since again, we note that the results for particle acceleration are very similar to the more evolved snapshots (see Figures 7 and 9). Finally, with regard to $t = 40\ L/c$, in this snapshot, which is just before the CDK turbulence reaches the nearly steady-state regime, we see that though the exponential growth of the particle kinetic energy is similar to the evolved nearly stationary snapshots, the number of particles that achieve the maximum energy is much smaller (Figure 5, top), which may reflect the (minor) effects of neglecting the plasma background evolution in this case.

Other interesting implications arise from the conversion of the simulations into physical units. The results from Figures 5, 8, 9, 12, and 13 imply a total acceleration time (including the exponential acceleration regime by reconnection plus the slower final drift acceleration) of approximately a few thousand hours. During this time, particles have reentered the system across the periodic boundaries in the longitudinal direction (z) several times, traveling a total length of the order of $\sim 10^{-1}$ pc along the jet. If we consider only the time elapsed during the acceleration exponential regime, the length scales are even smaller ($\sim 10^{-2}$ pc). These physical length scales characterize the size of the turbulent induced reconnection dissipation region where particles are accelerated, and, within these (time and length) scales, the physical conditions in a real system are not expected to change substantially, except for the dissipation of the magnetic energy. It is interesting to note that these scales are also compatible with estimates of the size of the reconnection dissipation layer considered in recent blazar jet studies (see, e.g., Christie et al. 2019; Giannios & Uzdensky 2019).

Besides the works above, other recent studies have also numerically explored acceleration by reconnection in relativistic jets but considering PIC simulations (e.g., Davelaar et al. 2020; Nishikawa et al. 2020). Christie et al. (2019) scaled the results of 2D PIC simulations of current sheets with the formation of plasmoids (or magnetic islands) of different sizes to the scales of relativistic jets. Coupling these plasmoid simulations with a radiative transfer code, they reproduced light curves of blazar sources, showing the efficiency of reconnection acceleration to explain multiscale variability in blazars across the entire EM spectrum. Nishikawa et al. (2020), on the other hand, performed 3D PIC simulations of a magnetically dominated relativistic jet of electron–proton pairs accounting for several mechanisms driving turbulence inside the jet and also found that magnetic reconnection should be the dominant acceleration process. Davelaar et al. (2020) achieved the same conclusion. However, none of these studies involving global jet simulations have derived the properties of the reconnection sites and their correlation with the accelerated particles, as in this work. Moreover, none of them obtained the general properties of particle acceleration, like the acceleration rate, the size of the acceleration region, and the saturation energy achieved by the particles. With regard to the spectrum, Davelaar et al. (2020) obtained a much steeper power-law index than in this work, probably due to the higher magnetization of their jet model, and Nishikawa et al. (2020) did not obtain any power-law index due to the limited resolution.

It is remarkable that in our work, though we have considered a mild magnetization parameter (~ 1 in the evolved jet), the results are very consistent, even with PIC studies with much higher magnetization (e.g., Comisso & Sironi 2018, 2019). For instance, the hardness of the power spectrum of the particles in our simulations, in spite of the intrinsic limitations of the test particle method, is similar to these studies. In contrast, as remarked above, Davelaar et al. (2020) obtained a much steeper power spectrum (the larger the magnetization parameter, the steeper the slope), which they interpreted as due to an inhibition of the acceleration by the strong guide field of the

plasma. Comisso & Sironi (2018, 2019), on the other hand, interpreted their very hard spectrum (which improves with increasing magnetization) as due to the high amplitude of the turbulent fluctuations that are accelerating the particles (though turbulence is decaying in their simulations), and in this way, the underlying magnetic field is not sufficient to kill the stochastic process. Therefore, it is possible that one may obtain similar results when considering MHD relativistic jets with higher magnetization, as long as the amplitude of the magnetic fluctuations of the driving turbulence is kept large enough (i.e., $\delta B/B \sim 1$, as, e.g., in Comisso & Sironi 2018, 2019). This obviously requires further investigation, since a critical difference between our study and that of Comisso & Sironi (2018, 2019) is the absence in their case of an underlying strong large-scale magnetic field, like we have in the jet (see also Kowal et al. 2012; de Gouveia Dal Pino & Kowal 2015).

As mentioned before, another recent study also explored particle acceleration in relativistic jets subject to the CDK instability by means of 3D PIC simulations of electron–positron pairs (Alves et al. 2018). These authors examined the early nonlinear development of this instability and identified an acceleration of the particles due to curvature drift in the wiggling magnetic field structure of growing amplitude along the jet spine. According to their results, a maximum energy growth rate for the electrons $(\Delta E/\Delta t)/(m_e c^2) \sim 12\ c/R$ is achieved at the maximum energy to which the particles are accelerated, $\sim 125\ m_e c^2$, where R is the jet radius and the energy is normalized by the electron rest mass energy (see Figure 3(d) in Alves et al. 2018). This implies an acceleration time for the electrons of $t_{\rm acc,e} \simeq 10.4\ R/c$. Considering our test particle model in the earlier jet snapshot, where we also identified curvature drift acceleration, i.e., $t = 25\ L/c$ (model ut25), Figure 9 (bottom panel) gives for this model a maximum energy growth rate for the protons of $(\Delta E/\Delta t)/(m_p c^2) \sim 10^5\ {\rm hr}^{-1}$, which is achieved at a saturation energy of $\sim 5 \times 10^6\ m_p c^2$. This implies an acceleration time for the protons of $t_{\rm acc,p} \simeq 50$ hr. In order to compare both rates, we need to estimate the acceleration time for the electrons in our simulation. In the relativistic regime, the acceleration time for electrons is approximately given by $t_{\rm acc,e} \simeq t_{\rm acc,p}(m_e/m_p)$ (e.g., Khiali et al. 2015). Thus, from our results, we might expect an electron acceleration time up to the saturation energy due to curvature drift of the order of $t_{\rm acc,e} \simeq 100$ s, which is comparable to the one obtained in Alves et al. (2018) if one considers a jet radius $R \sim 10^{-7}$ pc in their PIC simulation. However, this is only a rough estimate, since the scales implied in the two simulations are rather distinct.[13] Moreover, in order to improve our estimate for electrons, we should also perform numerical simulations for them. However, the numerical integration of the electron trajectories is much longer than for protons in MHD domains and computationally expensive.

Finally, we should remark that in situ particle acceleration examined directly in real systems, like the 3D relativistic jets we considered here, is a very promising approach because it allows for testing the process under more realistic environmental conditions, with turbulence and reconnection driven by natural physical processes, allowing for direct applications to observed systems and even including time-dependence effects. The comparisons with former studies in single current sheets have further validated the process, confirming its ubiquitous nature. The similarity of our results with these earlier works that are based on local (higher-resolution) simulations of current sheets (in both PIC and MHD +test particle simulations) have served not only to benchmark and validate our results but also to highlight the stochastic and universal nature of the process across the scales. Furthermore, this method of injecting particles directly into the collisional MHD simulation of the relativistic jet has allowed the acceleration of the particles up to the real physical scales, i.e., up to the observed ultra-high-energy values. This is without the need to extrapolate the much smaller energies that are achieved in the kinetic scales to the large scales, as it is required in PIC simulations. In forthcoming work, we intend to include the radiative losses of the particles and apply them to observed systems. Moreover, since our MHD collisional approach has limitations, as only injected particles with a Larmor radius close to the MHD scales can be effectively accelerated, and they allow only for modest values of the magnetization parameter, future studies involving hybrid simulations combining PIC and MHD approaches, like those performed for single current sheets (e.g., Bai et al. 2015), should also be applied to real systems, probing both the kinetic and macroscopic scales of the process and accounting for particle feedback in the system.

T.E.M.T. acknowledges support from the Brazilian Agency CAPES, E.M.d.G.D.P. from the Brazilian Funding Agencies FAPESP (grant 13/10559-5) and CNPq (grant 308643/2017-8), L.K. from FAPESP (2016/12320-8), and G.K. from CNPq (grant 304891/2016-9) and FAPESP (grants 2013/10559-5 and 2019/03301-8). C.B.S. is supported by the National Natural Science Foundation of China under grant No. 12073021. Y.M. is supported by the ERC Synergy Grant "BlackHoleCam: Imaging the Event Horizon of Black Holes" (grant No. 610058). The simulations presented in this work were performed in the cluster of the Group of Plasmas and High-Energy Astrophysics (GAPAE), acquired with support from FAPESP (grant 2013/10559-5), in the Blue Gene/Q supercomputer supported by the Center for Research Computing (Rice University) and Superintendência de Tecnologia da Informação da Universidade de São Paulo (USP) and the computing facilities of the Laboratory of Astroinformatics (IAG/USP, NAT/Unicsul), whose purchase was also made possible by FAPESP (grant 2009/54006-4) and the INCT-A. The authors are also grateful to an anonymous referee whose comments have helped to improve the paper.

ORCID iDs

Tania E. Medina-Torrejón https://orcid.org/0000-0003-4666-1843
Elisabete M. de Gouveia Dal Pino https://orcid.org/0000-0001-8058-4752
Luis H. S. Kadowaki https://orcid.org/0000-0002-6908-5634
Grzegorz Kowal https://orcid.org/0000-0002-0176-9909
Chandra B. Singh https://orcid.org/0000-0002-7782-5719
Yosuke Mizuno https://orcid.org/0000-0002-8131-6730

References

Aartsen, M., Ackermann, M., Adams, J., et al. 2018, Sci, 361, 147
Abramowicz, M. A., & Fragile, P. C. 2013, LRR, 16, 1
Ackermann, M., Anantua, R., Asano, K., et al. 2016, ApJL, 824, L20
Aharonian, F., Akhperjanian, A. G., Bazer-Bachi, A. R., et al. 2007, ApJL, 664, L71

[13] As remarked, considering the conversion in physical units adopted in our simulations, where the time unit is 1 hr, this implies a physical unit length in our jet of $L = c\ t \sim 10^{-4}$ pc.

Albert, J., Aliu, E., Anderhub, H., et al. 2007, ApJL, 665, L51
Alves, E. P., Zrake, J., & Fiuza, F. 2018, PhRvL, 121, 245101
Bai, X.-N., Caprioli, D., Sironi, L., & Spitkovsky, A. 2015, ApJ, 809, 55
Barniol Duran, R., Tchekhovskoy, A., & Giannios, D. 2017, MNRAS, 469, 4957
Begelman, M. C. 1998, ApJ, 493, 291
Begelman, M. C., Fabian, A. C., & Rees, M. J. 2008, MNRAS, 384, L19
Bell, A. R. 1978, MNRAS, 182, 147
Bell, A. R., Araudo, A. T., Matthews, J. H., & Blundell, K. M. 2018, MNRAS, 473, 2364
Beresnyak, A., & Li, H. 2016, ApJ, 819, 90
Blandford, R., & Eichler, D. 1987, PhR, 154, 1
Blandford, R. D., & Payne, D. G. 1982, MNRAS, 199, 883
Blandford, R. D., & Znajek, R. L. 1977, MNRAS, 179, 433
Boccardi, B., Krichbaum, T., Bach, U., Ros, E., & Zensus, J. A. 2015, arXiv:1504.01272
Britto, R. J., Bottacini, E., Lott, B., Razzaque, S., & Buson, S. 2016, ApJ, 830, 162
Bromberg, O., Singh, C. B., Davelaar, J., & Philippov, A. A. 2019, ApJ, 884, 39
Bromberg, O., & Tchekhovskoy, A. 2016, MNRAS, 456, 1739
Brunetti, G., & Lazarian, A. 2011, MNRAS, 410, 127
Brunetti, G., & Vazza, F. 2020, PhRvL, 124, 051101
Cerruti, M. 2020, JPhCS, 1468, 012094
Cerutti, B., Uzdensky, D. A., & Begelman, M. C. 2012, ApJ, 746, 148
Cerutti, B., Werner, G. R., Uzdensky, D. A., & Begelman, M. C. 2014, PhPl, 21, 056501
Christie, I. M., Petropoulou, M., Sironi, L., & Giannios, D. 2019, MNRAS, 482, 65
Clausen-Brown, E., & Lyutikov, M. 2012, MNRAS, 426, 1374
Comisso, L., & Sironi, L. 2018, PhRvL, 121, 255101
Comisso, L., & Sironi, L. 2019, ApJ, 886, 122
Das, U., & Begelman, M. C. 2019, MNRAS, 482, 2107
Davelaar, J., Philippov, A. A., Bromberg, O., & Singh, C. B. 2020, ApJL, 896, L31
de Gouveia Dal Pino, E., Batista, R. A., Kadowaki, L. H. S., et al. 2018, in Int. Conf. on Black Holes as Cosmic Batteries: UHECRs and Multimessenger Astronomy, ed. R. Cassia Anjos & C. H. Coimbra Araujo (Trieste: Proceedings of Science), 8
de Gouveia Dal Pino, E. M., & Kowal, G. 2015, in Astrophysics and Space Science Library, Vol. 407, Particle Acceleration by Magnetic Reconnection, ed. A. Lazarian, E. M. de Gouveia Dal Pino, & C. Melioli (Berlin: Springer), 373
de Gouveia Dal Pino, E. M., Kowal, G., Kadowaki, L., et al. 2020, in IAU Symp. 342, Perseus in Sicily: From Black Hole to Cluster Outskirts, ed. K. Asada et al. (Cambridge: Cambridge Univ. Press), 13
de Gouveia Dal Pino, E. M., Kowal, G., Kadowaki, L. H. S., Piovezan, P., & Lazarian, A 2010a, IJMPD, 19, 729
de Gouveia Dal Pino, E. M., & Lazarian, A. 2005, A&A, 441, 845
de Gouveia Dal Pino, E. M., Piovezan, P. P., & Kadowaki, L. H. S. 2010b, A&A, 518, A5
del Valle, M. V., de Gouveia Dal Pino, E. M., & Kowal, G. 2016, MNRAS, 463, 4331
Doeleman, S. S., Fish, V. L., Schenck, D. E., et al. 2012, Sci, 338, 355
Drake, J. F., Opher, M., Swisdak, M., & Chamoun, J. N. 2010, ApJ, 709, 963
Drake, J. F., Swisdak, M., Che, H., & Shay, M. A. 2006, Natur, 443, 553
Drake, J. F., Swisdak, M., & Fermo, R. 2013, ApJL, 763, L5
Drenkhahn, G., & Spruit, H. C. 2002, A&A, 391, 1141
Drury, L. O. 2012, MNRAS, 422, 2474
Eyink, G. L., Lazarian, A., & Vishniac, E. T. 2011, ApJ, 743, 51
Fowler, T. K., Li, H., & Anantua, R. 2019, ApJ, 885, 4
Giannios, D. 2008, A&A, 480, 305
Giannios, D. 2010, MNRAS, 408, L46
Giannios, D. 2013, MNRAS, 431, 355
Giannios, D., & Spruit, H. C. 2006, A&A, 450, 887
Giannios, D., & Spruit, H. C. 2007, A&A, 469, 1
Giannios, D., & Uzdensky, D. A. 2019, MNRAS, 484, 1378
Giannios, D., Uzdensky, D. A., & Begelman, M. C. 2009, MNRAS, 395, L29
Gill, R., Granot, J., & Lyubarsky, Y. 2018, MNRAS, 474, 3535
Giroletti, M., Giovannini, G., Feretti, L., et al. 2004, ApJ, 600, 127
Guo, F., Li, H., Daughton, W., Li, X., & Liu, Y.-H. 2016, PhPl, 23, 055708
Guo, F., Li, H., Daughton, W., & Liu, Y.-H. 2014, PhRvL, 113, 155005
Guo, F., Liu, Y.-H., Daughton, W., & Li, H. 2015, ApJ, 806, 167
Hardee, P., Mizuno, Y., & Nishikawa, K.-I. 2007, Ap&SS, 311, 281
Harris, D. E., Biretta, J. A., Junor, W., et al. 2003, ApJL, 586, L41
Hovatta, T., & Lindfors, E. 2019, NewAR, 87, 101541
Kadowaki, L. H. S., de Gouveia Dal Pino, E., & Medina-Torrejon, T. E. 2018a, in Int. Conf. on Black Holes as Cosmic Batteries: UHECRs and Multimessenger Astronomy, ed. R. Cassia Anjos & C. H. Coimbra Araujo (Trieste: Proceedings of Science), 16
Kadowaki, L. H. S., de Gouveia Dal Pino, E. M., Medina Torrejon, T. E., Mizuno, Y., & Kushwaha, P. 2020, arXiv:2011.03634
Kadowaki, L. H. S., de Gouveia Dal Pino, E. M., & Singh, C. B. 2015, ApJ, 802, 113
Kadowaki, L. H. S., de Gouveia Dal Pino, E. M., & Stone, J. M. 2018b, ApJ, 864, 52
Khiali, B., de Gouveia Dal Pino, E. M., & del Valle, M. V. 2015, MNRAS, 449, 34
Kovalev, Y. Y., Lister, M. L., Homan, D. C., & Kellermann, K. I. 2007, ApJL, 668, L27
Kowal, G., de Gouveia Dal Pino, E. M., & Lazarian, A. 2011, ApJ, 735, 102
Kowal, G., de Gouveia Dal Pino, E. M., & Lazarian, A. 2012, PhRvL, 108, 241102
Kowal, G., Lazarian, A., Vishniac, E. T., & Otmianowska-Mazur, K. 2009, ApJ, 700, 63
Kushwaha, P., Sinha, A., Misra, R., Singh, K. P., & de Gouveia Dal Pino, E. M. 2017, ApJ, 849, 138
Laurent, P., Rodriguez, J., Wilms, J., et al. 2011, Sci, 332, 438
Lazarian, A., Eyink, G. L., Jafari, A., et al. 2020, PhPl, 27, 012305
Lazarian, A., & Vishniac, E. T. 1999, ApJ, 517, 700
Lazarian, A., Vlahos, L., Kowal, G., et al. 2012, SSRv, 173, 557
Li, X., Guo, F., Li, H., & Li, G. 2015, ApJL, 811, L24
Lobanov, A. P., & Zensus, J. A. 2001, Sci, 294, 128
Lyubarsky, Y., & Kirk, J. G. 2001, ApJ, 547, 437
Lyubarsky, Y., & Liverts, M. 2008, ApJ, 682, 1436
Lyutikov, M., Sironi, L., Komissarov, S. S., & Porth, O. 2017, JPlPh, 83, 635830602
Martí-Vidal, I., Muller, S., Vlemmings, W., Horellou, C., & Aalto, S. 2015, Sci, 348, 311
Matthews, J., Bell, A., & Blundell, K. 2020, NewAR, 89, 101543
McKinney, J. C. 2006, MNRAS, 368, 1561
McKinney, J. C., & Uzdensky, D. A. 2012, MNRAS, 419, 573
Mizuno, Y., Gómez, J. L., Nishikawa, K.-I., et al. 2015, ApJ, 809, 38
Mizuno, Y., Hardee, P. E., & Nishikawa, K.-I. 2011, ApJ, 734, 19
Mizuno, Y., Hardee, P. E., & Nishikawa, K.-I. 2014, ApJ, 784, 167
Mizuno, Y., Lyubarsky, Y., Nishikawa, K.-I., & Hardee, P. E. 2009, ApJ, 700, 684
Mizuno, Y., Lyubarsky, Y., Nishikawa, K.-I., & Hardee, P. E. 2012, ApJ, 757, 16
Mizuno, Y., Nishikawa, K.-I., Koide, S., Hardee, P., & Fishman, G. J. 2006, arXiv:astro-ph/0609004
Nagai, H., Haga, T., Giovannini, G., et al. 2014, ApJ, 785, 53
Nathanail, A., Fromm, C. M., Porth, O., et al. 2020, MNRAS, 495, 1549
Nishikawa, K., Mizuno, Y., Gómez, J. L., et al. 2020, MNRAS, 493, 2652
Porth, O., & Komissarov, S. S. 2015, MNRAS, 452, 1089
Rodriguez-Ramirez, J. C., de Gouveia Dal Pino, E. M., & Alves Batista, R. 2019, ApJ, 879, 6
Santos-Lima, R., Guerrero, G., de Gouveia Dal Pino, E. M., & Lazarian, A. 2020, arXiv:2005.07775
Santos-Lima, R., Lazarian, A., de Gouveia Dal Pino, E. M., & Cho, J. 2010, ApJ, 714, 442
Singh, C. B., de Gouveia Dal Pino, E. M., & Kadowaki, L. H. S. 2015, ApJL, 799, L20
Singh, C. B., Mizuno, Y., & de Gouveia Dal Pino, E. M. 2016, ApJ, 824, 48
Sironi, L., Petropoulou, M., & Giannios, D. 2015, MNRAS, 450, 183
Sironi, L., & Spitkovsky, A. 2014, ApJL, 783, L21
Sironi, L., Spitkovsky, A., & Arons, J. 2013, ApJ, 771, 54
Spruit, H. C., Daigne, F., & Drenkhahn, G. 2001, A&A, 369, 694
Striani, E., Mignone, A., Vaidya, B., Bodo, G., & Ferrari, A. 2016, MNRAS, 462, 2970
Takamoto, M., Inoue, T., & Lazarian, A. 2015, ApJ, 815, 16
Tchekhovskoy, A., & Bromberg, O. 2016, MNRAS, 461, L46
Werner, G. R., Philippov, A. A., & Uzdensky, D. A. 2019, MNRAS, 482, L60
Werner, G. R., Uzdensky, D. A., Begelman, M. C., Cerutti, B., & Nalewajko, K. 2018, MNRAS, 473, 4840
Yuan, F., & Narayan, R. 2014, ARA&A, 52, 529
Zenitani, S., & Hoshino, M. 2001, Apjl, 562, L63
Zenitani, S., & Hoshino, M. 2007, ApJ, 670, 702
Zenitani, S., & Hoshino, M. 2008, ApJ, 677, 530
Zhang, B., & Yan, H. 2011, ApJ, 726, 90
Zhdankin, V., Uzdensky, D. A., Perez, J. C., & Boldyrev, S. 2013, ApJ, 771, 124
Zweibel, E. G., & Yamada, M. 2009, ARA&A, 47, 291